



RESEARCH ARTICLE

10.1029/2019JF005424

Special Section:

The Arctic: An AGU Joint Special Collection

Thermokarst Lake to Lagoon Transitions in Eastern Siberia: Do Submerged Taliks Refreeze?

Michael Angelopoulos^{1,2} , Pier Paul Overduin¹ , Sebastian Westermann³ , Jens Tronicke² , Jens Strauss¹ , Lutz Schirrmeister¹ , Boris K. Biskaborn¹ , Susanne Liebner^{4,5} , Georgii Maksimov⁶ , Mikhail N. Grigoriev⁶ , and Guido Grosse^{1,2} 

¹Alfred Wegener Institute, Helmholtz Centre for Polar and Marine Research, Potsdam, Germany, ²University of Potsdam, Institute of Geosciences, Potsdam, Germany, ³Department of Geosciences, University of Oslo, Oslo, Norway, ⁴GFZ German Research Centre for Geosciences, Section Geomicrobiology, Potsdam, Germany, ⁵University of Potsdam, Institute of Biogeochemistry and Biology, Potsdam, Germany, ⁶Melnikov Permafrost Institute, Siberian Branch of the Russian Academy of Sciences, Yakutsk, Russia

Key Points:

- Thermokarst lake taliks may refreeze when inundated with seawater, even under floating ice conditions
- Salt rejection from lagoon ice formation and seasonal isolation from the sea cause hypersaline conditions below the lagoon's ice cover
- Subaquatic ice-bearing permafrost formation suggests that not all subsea ice-bearing permafrost is former terrestrial permafrost

Supporting Information:

- Supporting Information S1

Correspondence to:

M. Angelopoulos,
michael.angelopoulos@awi.de

Citation:

Angelopoulos, M., Overduin, P. P., Westermann, S., Tronicke, J., Strauss, J., Schirrmeister, L., et al. (2020). Thermokarst lake to lagoon transitions in eastern Siberia: Do submerged taliks refreeze? *Journal of Geophysical Research: Earth Surface*, 125, e2019JF005424. <https://doi.org/10.1029/2019JF005424>

Received 2 NOV 2019

Accepted 22 JUN 2020

Accepted article online 20 JUL 2020

Corrected 29 OCT 2020

This article was corrected on 29 OCT 2020. See the end of the full text for details.

©2020. The Authors.

This is an open access article under the terms of the Creative Commons Attribution License, which permits use, distribution and reproduction in any medium, provided the original work is properly cited.

As the Arctic coast erodes, it drains thermokarst lakes, transforming them into lagoons, and, eventually, integrates them into subsea permafrost. Lagoons represent the first stage of a thermokarst lake transition to a marine setting and possibly more saline and colder upper boundary conditions. In this research, borehole data, electrical resistivity surveying, and modeling of heat and salt diffusion were carried out at Polar Fox Lagoon on the Bykovsky Peninsula, Siberia. Polar Fox Lagoon is a seasonally isolated water body connected to Tiksi Bay through a channel, leading to hypersaline waters under the ice cover. The boreholes in the center of the lagoon revealed floating ice and a saline cryotic bed underlain by a saline cryotic talik, a thin ice-bearing permafrost layer, and unfrozen ground. The bathymetry showed that most of the lagoon had bedfast ice in spring. In bedfast ice areas, the electrical resistivity profiles suggested that an unfrozen saline layer was underlain by a thick layer of refrozen talik. The modeling showed that thermokarst lake taliks can refreeze when submerged in saltwater with mean annual bottom water temperatures below or slightly above 0°C. This occurs, because the top-down chemical degradation of newly formed ice-bearing permafrost is slower than the refreezing of the talik. Hence, lagoons may precondition taliks with a layer of ice-bearing permafrost before encroachment by the sea, and this frozen layer may act as a cap on gas migration out of the underlying talik.

1. Introduction

Borehole observations over 10 years (2007–2016) showed that subaerial permafrost is warming rapidly at a global scale even at depths greater than 10 m (Biskaborn et al., 2019). Taliks (unfrozen ground within permafrost) that develop on land may play a critical role in determining the response of permafrost after inundation from the sea (Shakhova et al., 2017). Subsea permafrost underlies almost 2.5×10^6 km² of the Arctic shelves (Overduin et al., 2019) and contains old frozen organic carbon stocks (Strauss et al., 2013; Vonk et al., 2012), which have been thawing since the last deglaciation. Recent research estimates that approximately 1.6 kg/m²/year of subsea permafrost organic carbon thaws out on the East Siberian Arctic Shelf close to Muostakh Island (Wild et al., 2018). Through microbial degradation, the organic matter can transform to carbon dioxide or methane and be released to the water column. Greenhouse gas that is ultimately emitted to the atmosphere may act as a positive feedback to climate warming (Schuur et al., 2015; Shakhova et al., 2010). Methane gas hydrates are also present in subsea permafrost and exist at shallower depths compared to typical marine environments (Riedel et al., 2017). The methane hydrates are embedded within the ice-bearing sediment or below the bottom of the permafrost. Methane may also exist in a dissolved phase in the porewater or as free gas within or below the ice-bearing sediment. Thus, thawing subsea permafrost from warming and salt transport may degrade gas hydrates (Chuvilin et al., 2019) and increase the gas permeability of ice-bearing sediment (Chuvilin et al., 2016) to trigger gas migration toward the seabed. Gas migration would be facilitated by the presence of open taliks. These pathways could exist where deep taliks below thermokarst lakes or paleo-river valleys are inundated with seawater (Frederick & Buffett, 2014; Nicolsky & Shakhova, 2010; Shakhova et al., 2017). However, the fate of submerged taliks after a freshwater to saltwater transition is uncertain. It has been suggested seawater with negative mean annual bottom water temperatures refreezes

taliks (Romanovskii et al., 2000, 2004), but not if salt is transported into the sediment fast enough to lower the freezing point of the sediment porewater. With numerical modeling, Malakhova (2016) showed the effects of thermokarst lake taliks on the gas hydrate stability zone's evolution after transgression and that seawater can partially refreeze taliks from the top. However, the coupled effects of heat and salt flow were not included in the simulations. While heat diffusion is typically faster than salt diffusion, the convective transport of salt can be rapid in coarse-grained sediments (Harrison & Osterkamp, 1978, 1982). In the Dmitry Laptev Strait, Shakhova et al. (2017) observed submerged thaw-lake basins with high-resolution seismic imagery. These basins were associated with pockmarks on the seabed and increased concentrations of dissolved methane in the water column, suggesting that the submerged talik did not refreeze and was a flowpath for ascending gas. Marine seismic surveys have also identified former thermokarst lake basins infilled with lagoonal and marine sediment (Rekant et al., 2015), and lagoons can salinize subaquatic thermokarst lake taliks (Romanovskii et al., 2004). Thus, the refreezing of taliks after inundation may depend on local subaquatic conditions.

More generally, subaquatic permafrost includes permafrost below seas, lakes, and lagoons. Subaquatic permafrost thawing and freezing depend on the duration of inundation, warming or cooling rate, the coupling of the bed to the atmosphere through bedfast ice, and salt transport into the sediments (Overduin et al., 2012). The impact of salt transport depends on the salinity of the water, which can vary seasonally.

In the Arctic, lagoons support diverse food webs and provide habitat and feeding grounds for many species (Harris et al., 2018). In addition, they sequester large amounts of organic carbon released to the nearshore zone from eroding permafrost coasts (Grotheer et al., 2020). Lagoons are widespread features along Arctic coasts and characterize more than 70% of the eastern Beaufort Sea, for example (Harris et al., 2017). In shallow water, bedfast ice can isolate lagoons from the sea and create pockets of hypersaline water under floating ice (Harris et al., 2017; Schell, 1974). Even in the case of a 60 m-deep lake in the Canadian High Arctic with a seasonal connection to the sea, the isolation of the lake in winter and spring results in hypersaline conditions due to brine rejection from lake ice formation after multiple years (Dugan & Lamoureaux, 2011). Hypersaline conditions in winter and spring also develop in offshore subsea permafrost areas where the water circulation is restricted below the ice (Grigoriev, 2008; Osterkamp, 2001). For example, Sellmann (1989) reported bottom water temperatures lower than -3°C in Harrison Bay, Alaska. Despite the potential for hypersaline cryotic conditions below the ice cover, lagoons are susceptible to the rapid flushing of saltwater in spring after ice breakup and fluvial freshwater inflows (Matthews & Stringer, 1984). Furthermore, Harris et al. (2017) showed that lagoons can have dramatic annual variations in temperature and salinity. The temperature can range from -2°C to 14°C and the salinity from 0 practical salinity units (psu) to over 45 psu. These variations are affected by the lagoon's connectivity to the sea. Connectivity to the sea, evaporation, and freshwater inputs are all important controls on the development of hypersalinity for lagoons in both Arctic and non-Arctic regions (Tweedley et al., 2019).

A thermokarst lagoon is an intermediate stage between a thermokarst lake and the sea. We investigated the transition from a freshwater to a saltwater system at Polar Fox Lagoon on the southern Bykovsky Peninsula, northeastern Siberia. Polar Fox Lagoon was chosen because it represents a partially drained thermokarst lake affected by seawater influx through a channel but is not yet bisected by the coastline. That is to say, the lake's transition had begun, but it is not yet part of the marine setting. Along Arctic coasts with brackish seawater, we hypothesize that lagoons can generate seasonally cryotic and hypersaline conditions and refreeze thermokarst lake taliks. The objective of this paper is to combine observational data on a thermokarst lagoon's permafrost distribution and composition with the results of numerical modeling in order to determine if submerged thermokarst lake taliks can refreeze. Since the Polar Fox basin is partially drained, investigating the talik's response to seawater may offer insights regarding the evolution of submerged taliks on the shelf from rising sea levels since the last deglaciation.

2. Study Site

The Bykovsky Peninsula is located southeast of the Lena Delta in the Buor-Khaya Gulf of the Laptev Sea in northeastern Siberia, Russia. Like nearby Muostakh Island, the peninsula is an erosional remnant of an accumulation plain that began to form in the late Pleistocene (Grosse et al., 2007). The mean annual temperature at the depth of zero annual amplitude (approximately 20 m) in the hills not affected by

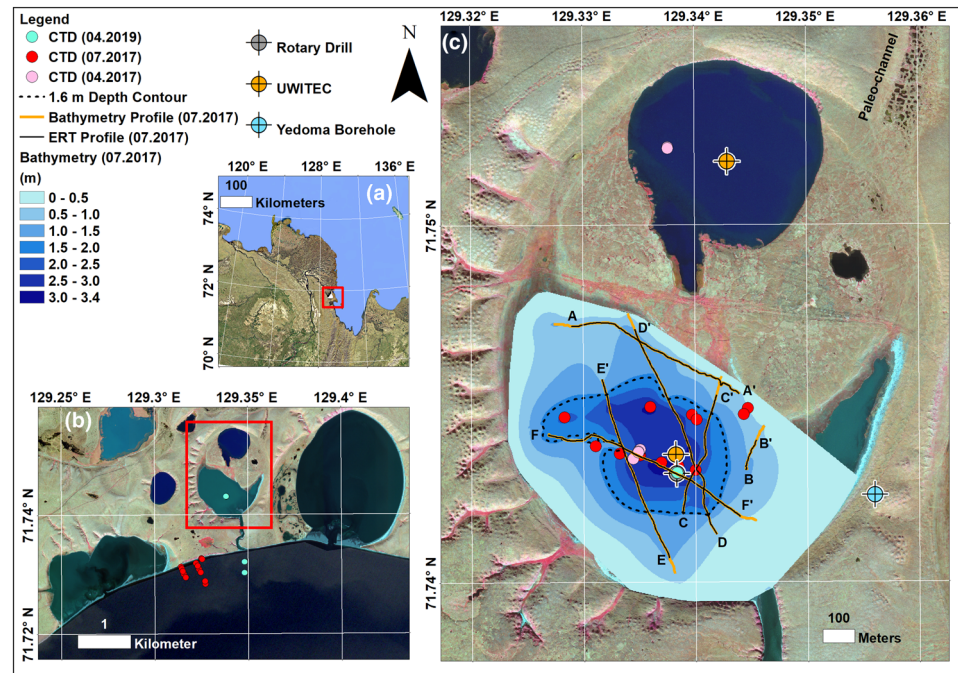


Figure 1. (a) The location of Polar Fox Lagoon on the Bykovsky Peninsula. (b) Polar Fox Lagoon bounded by Uomullyakh Lagoon toward the west and Ivashkina Lagoon toward the east. (c) Polar Fox Lagoon and Northern Polar Fox Lake. For panels b and c, the background is a high-resolution satellite image (30 cm ground resolution WorldView-3 image from 2 September 2016, ©Digital Globe).

thermokarst is -10°C (Schirrneister et al., 2018). Therefore, the permafrost can be hundreds of meters thick (Nicolosky et al., 2012). However, ground temperature near the depth of zero annual amplitude in the Arctic continuous permafrost zone increased by $0.39 \pm 0.15^{\circ}\text{C}$ between 2007 and 2016 and the warming trend is believed to continue (Biskaborn et al., 2019). An important feature of the permafrost is the Yedoma Ice Complex, which ranges from 45 m above sea level in the highlands to 15 m below sea level (Grigoriev, 1993; Grosse et al., 2007). The sediments within the Yedoma Ice Complex at or below sea level generally range from silty fine-grained sand to medium-grained sand (Grosse et al., 2007; Schirrneister et al., 2002). The total ice content, including ice wedges and intrasedimentary ice, can reach 87% by volume (Günther et al., 2015). As the climate warmed in the Late Glacial and early Holocene, widespread permafrost thawing and thermokarst development occurred (Biskaborn et al., 2013; Grosse et al., 2007; Kaplina, 2009). As sea levels rose from global deglaciation to inundate low-lying basins, shelves, and thermokarst lakes, the present-day landscape of the peninsula emerged (Bauch et al., 2001; Romanovskii et al., 2000). Coastal erosion has also shaped the coastline and continues to create new subsea permafrost. On the Bykovsky Peninsula, the coastal erosion rate is related to the coastal geomorphology (e.g., Yedoma Ice Complex cliff, Alas, thaw slump, sand bar, and lagoon barrier) and the orientation of the shoreline (Lantuit et al., 2011).

On the Bykovsky Peninsula, subaquatic permafrost has been investigated in Ivashkina Lagoon by Ulyantsev, Bratskaya, et al. (2016); Ulyantsev, Romankevich, et al. (2016); Cheverev et al. (2007); and Schirrneister et al. (2018). Ivashkina (egg-shaped lagoon right of the red rectangle in Figure 1b) is the peninsula's largest lagoon, extending 2.5 km inland and 2 km wide with the inlet only 1.6 km east of Polar Fox Lagoon's channel. Ulyantsev, Bratskaya, et al. (2016) reported an ice-bearing permafrost (IBP) depth of 12 m below the sediment surface in the northwestern part of the lagoon in 2014. The drilled IBP table is probably characteristic of a thawing refrozen talik, since there was a period of subaerial exposure in between the thermokarst lake and lagoon stages (Schirrneister et al., 2018).

Field measurements were mainly performed in Polar Fox Lagoon, which is situated within a large partially drained thermokarst lake basin (Figure 1). The basin's smaller northern lake (Northern Polar Fox Lake) is

currently filled with freshwater and that characterizes the sediment as corroborated by electrical conductivity measurements of the porewater from a 5 m sediment core retrieved in April 2017. The first major drainage event likely occurred in the northeastern paleo-channel. The northeastern paleo-channel has refrozen sediments as evidenced by a dense network of ice wedge polygons on the valley floor. The denser the ice wedge intersection points, then the older the ice wedge network should be assuming homogeneous substrate and climatic conditions across space (Dutilleul et al., 2009). The more recent and dramatic drainage event occurred in the southern channel, which connects the lagoon to Tiksi Bay. The channel's development was possibly triggered by a thermo-erosional gully that formed following the degradation of ice wedges. These gullies can generate channel networks hundreds of meters long (D. Fortier et al., 2007). The chemical composition of ice cores from Polar Fox Lagoon in April 2017 suggests that once the lagoon ice reaches a thickness of 0.5 m, bedfast ice in the channel's shallowest areas inhibits water exchange with Tiksi Bay (Spangenberg et al., 2020). Hence, the lagoon is a seasonally isolated water body as also described by Dugan and Lamoureux (2011).

Polar Fox Lagoon was 67 ha in size and had a maximum water depth of 3.4 m in July 2017 (Figure 1c). In April 2017, the ice thickness ranged from 1.6 to 1.8 m in floating ice zones and the snow thickness from 0 to 0.2 m. Assuming a minimum ice thickness of 1.6 m, an interpolated bathymetry map from July 2017 suggests that at least 75% of the lagoon's surface area had bedfast ice in April 2017. Water temperature and salinity beneath the floating ice are likely to vary strongly from year to year depending on ice thickness and the salinity of the water prior to ice formation and isolation from Tiksi Bay. In the open water season, the warm and fresh discharge from the Lena River flows along the peninsula's southern coastline and into the lagoon and is a major contributor of organic matter to the Laptev Sea (Juhls et al., 2019).

3. Fieldwork

Two joint Russian-German expeditions were carried out in April 2017 and July to August 2017 as part of the Lena Delta 2017 research program. The 3-week spring campaign completed boreholes, ice cores, and electrical conductivity, temperature, and depth (CTD) casts in Uomullyakh Lagoon, Goltsovoye Lake, and Polar Fox Lagoon. In the summer, geoelectric surveys with floating electrodes were carried out at the same sites, as well as offshore areas (Angelopoulos et al., 2019). In April 2019, additional CTD casts were taken in Polar Fox Lagoon and Tiksi Bay. All CTD casts were made in the water with a SontekTM CastAway instrument.

3.1. Boreholes, Sediment Coring, and Instrumentation

In April 2017, a borehole was drilled 27.5 m below the seafloor (bsf) using a Russian rotary drill (RD). In this paper, seafloor and lagoon bed are used in an equivalent manner. Sediment cores were collected, logged, photographed, and stored frozen in thermally insulated boxes for their travel to Germany for further laboratory work. After drilling, a 19 m GeoPrecision temperature cable with an accuracy of 0.1°C and a resolution of 0.01°C was installed for 5 days. The cable had been calibrated by measuring sensor offsets in a 0°C water ice bath. It contained 20 sensor nodes spaced by 1 m, and the first node was located 0.1 m bsf. The temperatures were corrected for drilling heat effects following Lachenbruch et al. (1982). Additionally, we used an UWITEC piston corer operated from the ice cover to retrieve overlapping sediment cores with a composite depth of 5.5 m in Polar Fox Lagoon and 5.0 m in Northern Polar Fox Lake. Compared to the RD system, the sediment cores retrieved by piston coring technique were undisturbed. The cores were cut in 10 cm sections directly after retrieval to avoid hydrochemical vertical mixing. Sediment core pieces were hermetically and optically sealed and stored in thermally insulated boxes in a frozen state, which were returned to Germany for laboratory analyses.

After the samples were thawed, Rhizon samplers were used to extract the porewater of the RD cores. For the UWITEC cores, porewater was extracted from the samples using a hydraulic press. The porewater was then analyzed for pH and electrical conductivity. Fieldwork is reported in Strauss et al. (2018), and supplementary borehole data are available from Jenrich (2020).

3.2. Electrical Resistivity Surveys

Electrical resistivity tomography (ERT) with floating electrodes has shown to be an effective technique to detect the top of IBP in saline or brackish waters as demonstrated by Angelopoulos et al. (2019), Overduin et al. (2012, 2016), and Sellmann et al. (1989). ERT has also been used to detect seasonal permafrost

changes of coastal bluffs (Swarzenski et al., 2016), the impacts of deep lateral seawater intrusions on coastal permafrost degradation (Kasprzak et al., 2017), and thermokarst lake taliks (You et al., 2017). In summer, six surveys with floating electrodes were carried out using an IRISTM Syscal Pro Deep Marine system and a 48 V transmitter. A 120 m cable with floating electrodes (each separated by 10 m) was towed behind a small inflatable boat, and soundings were taken at 1 to 5 m intervals along selected profiles (Figure 1). The ERT system was equipped with a GPS and an echo sounder to record the position and water depth. Two current electrodes and 11 potential electrodes were used in a reciprocal Wenner-Schlumberger array. The array was quasi-symmetrical, and each vertical sounding had alternate electrode pairs that were slightly off center. The offset between the boat and the first potential electrode was approximately 10 m.

4. Heat and Salt Diffusion Modeling

4.1. General Framework

In this study, 1-D heat and salt flow was modeled using the version of CryoGrid2 from Angelopoulos et al. (2019) with the MATLAB ode45 solver (Shampine & Reichelt, 1997). This model version couples a heat diffusion model for permafrost soils by Westermann et al. (2013) with salt diffusion for saturated sediment. The model does not simulate water movement or nondiffusive mechanisms of salt transport. The porewater salt concentration is expressed as the molar concentration of all ions, c [mol/m³], in the unfrozen liquid water, $\theta_w(T,c)$, where T is temperature. The porewater salt concentration, c , is related to the bulk sediment salt concentration per unit volume, C , as $C = c\theta_w$. Following Dmitrenko et al. (2011), the effective salt diffusivity (d_s) is a function of the salt diffusion coefficient in seawater d_o , the volumetric unfrozen water content θ_w , and the sediment tortuosity τ as shown in Equation 1:

$$d_s = d_o \frac{\theta_w}{\tau}. \quad (1)$$

For simplicity, we employ the freezing characteristic of Dall'Amico et al. (2011) for nonsaline ground material and shift the onset of freezing T_f according to Equation 2:

$$T_f = \frac{-R(T_{m,FW})^2}{L_f} c. \quad (2)$$

This describes the depression of the freezing point of free water with unfrozen porewater salt concentration, c [mol/m³] for low salt concentrations. Here, R is the universal gas constant, $T_{m,FW} = 273.15$ K is the freezing point of free water, and L_f is the volumetric latent heat of fusion of water. While the freezing point depression is typically calculated using the molality of dissolved ions (Atkins et al., 2018), we use the molarity and treat L_f and the density of the solvent (water) as constants. In addition to salt diffusion, freezing would lead to salt enrichment in the remaining unfrozen water (i.e., increasing c), consecutively lowering T_f and thus shifting the assumed freezing characteristic further to negative values.

4.2. Thermokarst Lake to Lagoon Scenarios

The fate of a thermokarst lake under floating ice conditions was modeled for a range of lake to lagoon scenarios. The base case model was constrained by field data, including CTD profiles, as well as ice and snow thickness. The stratigraphy was based upon the RD borehole. Sediment deposition and erosion were ignored, so the stratigraphy was the same every year. The base case model assumed a surface porosity of 0.5 that decreased with depth to reflect the increasing compaction of sediments (Lee, 2005) but did not consider a sharp change in porosity at the silt/sand interface. The porosity was nearly constant in the upper 50 m of sediment (less than 2% change with depth) but decreased to 0.33 at a depth of 814 m (initial modeled permafrost base prior to the thermokarst lake spin-up phase). The different scenarios are presented in Table 1. We varied the maximum porosity of the sand, the salt diffusion coefficient, the snow thickness, the initial lagoon water salinity prior to lagoon ice formation, the mean annual air temperature, the maximum seawater temperature in summer, and the thermokarst lake spin-up time.

Table 1
Parameterization for Polar Fox Lake to Lagoon Model Runs

Scenario	MAAT (°C)	Max sea T_b (°C)	Salinity (psu)	Snow (m)	Max sand ϕ	Spin-up (years)	d_o (m^2/s)
1. Base case	-12.8	9.2	8.0	0.1	0.5	5,000	0.8×10^{-9}
2. Coarse sand	-12.8	9.2	8.0	0.1	0.3	5,000	0.8×10^{-9}
3. Windswept	-12.8	9.2	8.0	0.0	0.5	5,000	0.8×10^{-9}
4. Snowpack	-12.8	9.2	8.0	0.2	0.5	5,000	0.8×10^{-9}
5. Low salinity	-12.8	9.2	6.0	0.1	0.5	5,000	0.8×10^{-9}
6. High salinity	-12.8	9.2	12.0	0.1	0.5	5,000	0.8×10^{-9}
7. Cool winter	-13.8	9.2	8.0	0.1	0.5	5,000	0.8×10^{-9}
8. Warm winter	-11.8	9.2	8.0	0.1	0.5	5,000	0.8×10^{-9}
9. Cool sea	-12.8	8.2	8.0	0.1	0.5	5,000	0.8×10^{-9}
10. Warm sea	-12.8	10.2	8.0	0.1	0.5	5,000	0.8×10^{-9}
11. Cool talik	-12.8	9.2	8.0	0.1	0.5	1,000	0.8×10^{-9}
12. Rapid salt flow	-12.8	9.2	8.0	0.1	0.5	5,000	0.8×10^{-8}

Note. MAAT = mean annual air temperature; Max = maximum; T_b = bottom water temperature; Salinity = the lagoon salinity just prior to ice formation; Snow = maximum snow thickness; ϕ = porosity; and d_o = the salt diffusion coefficient.

4.3. Material Properties

For each scenario, 5 m of silt was underlain by sand, and the appropriate freezing characteristic curves for nonsaline sediment were assigned to each unit (Dall'Amico et al., 2011). The freezing curves were shifted based on the salt content in the unfrozen liquid water (Equation 2). The mineral thermal conductivity of silt was set to 3.0 W/(mK), and sand was set to 5.0 W/(mK) to reflect the higher quartz content of coarse-grained sediment (Williams & Smith, 1991), and the volumetric heat capacity was set to 2.0 MJ/(m³K) for both sediment types. Standard thermal properties for ice and water were used (Westermann et al., 2013), and the bulk thermal conductivity for a grid cell was calculated following Cosenza et al. (2003).

4.4. Model Spin-up

Polar Fox Lagoon originated as a freshwater thermokarst lake that had developed on terrestrial permafrost with a ground surface temperature of -10°C (Schirmer et al., 2018) and that persisted for 1,000 to 5,000 years prior to lagoon formation. The maximum spin-up time of 5,000 years is in line with the intense thermokarst development of the mid-Holocene (Grosse et al., 2007). We modeled varying lengths of time for the thermokarst lake period (before lagoon formation) to evaluate the effects of varying talik thickness and temperature. The spin-up model used a mean lakebed temperature of 3.0°C (Boike et al., 2015), and the initial salinity was set to zero everywhere in the model domain.

4.5. Boundary Conditions

For each simulation, the geothermal heat flux was set to 0.05 W/m². The upper boundary conditions were calculated independently and then used as an upper boundary forcing on the lagoon bed. Each model began in late September, the beginning of the lagoon ice season. The boundary conditions for the base case scenario are presented in Figure 2. The initial salinity of the water determines its freezing point and ice formation starts when the air temperature dips below this value. After the first day of ice formation, the snow thickness increased at a rate of 0.01 m/day until the maximum value shown in Table 1. We calculated the ice thickness based on a two-layer snow-ice system presented by Leppäranta (1993) using a thermal conductivity of 0.3 W/(mK) for snow. As ice builds, it is assumed that all salts are rejected into the water and that the temperature of the water is equal to the freezing point. For the first 0.5 m of ice formation, the salt content increases slowly as the lagoon is not yet isolated from Tiksi Bay (Spangenberg et al., 2020). After 0.5 m of ice formation, the lagoon is cut off from Tiksi Bay, and salt content increases rapidly. First, the bathymetry from July 2017 was interpolated in ESRI ArcGISTM using the natural neighbor method. Subsequently, we fit a polynomial function to liquid water volume versus ice thickness. At each time step, the change in ice thickness rejects salt into a smaller liquid water volume. However, the salt originally contained in newly formed bedfast ice zones is not added to the remaining liquid water. As a result, we fit a polynomial function to floating ice area versus ice thickness as well. The equation for the lagoon water salinity (c_w) is shown in

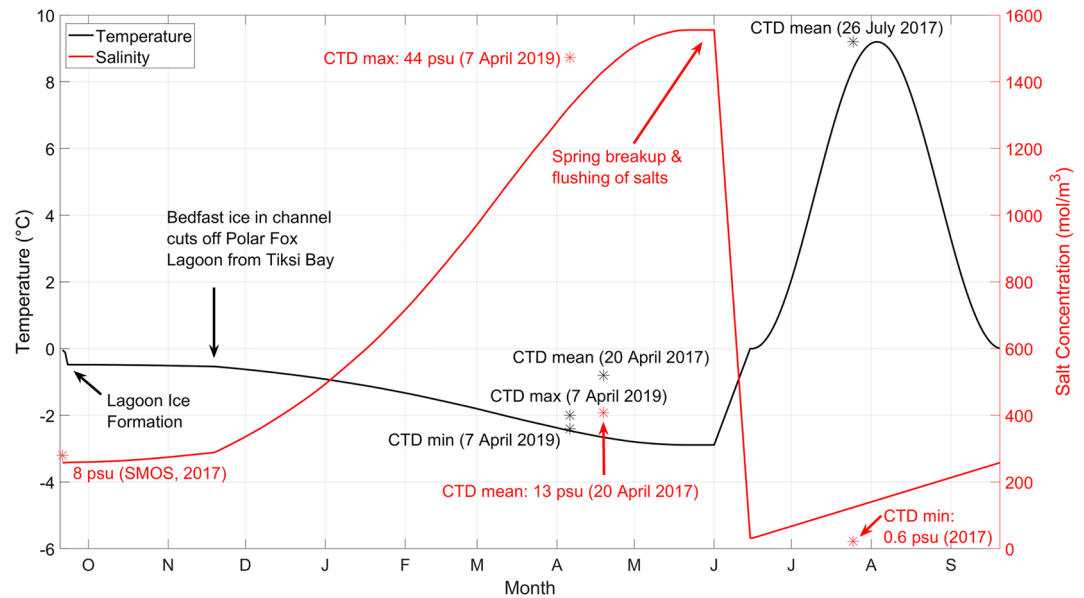


Figure 2. The upper boundary conditions for the base case scenario, using the relationship between bottom water temperature and salinity for the lagoon ice season. The model forcing is plotted together with available field observations. The Soil Moisture and Ocean Salinity (SMOS) data are described in Angelopoulos et al. (2019).

Equation 3, where V_w is the liquid water volume, A_{ice} is the surface area of floating ice, d_{ice} is the change in ice thickness, and t is time in days.

$$c_w(t) = \frac{c_w(t-1)[V_w(t) + A_{ice}(t)d_{ice}]}{V_w(t)} \quad (3)$$

When air temperatures increase to more than 0°C, spring breakup occurs. We assumed a 15-day breakup period, which is consistent with ice melt periods for thermokarst lakes in the Lena Delta (Boike et al., 2015). Therefore, the minimum bottom water temperature increased linearly for 15 days until 0°C, and the maximum bottom water salinity decreased linearly for 15 days until a minimum of 1 psu. For simplification, we assumed no lag between the increase in temperature and the decrease in salinity. The minimum salinity recorded with the CTD in July 2017 was 0.6 psu. After the breakup period, the bottom water temperatures varied as a sine function for the open water season with a maximum value of 9.2°C for the base case scenario. The mean water temperature recorded with the CTD in July 2017 was 9.2°C. After spring breakup, the bottom water salinity increased linearly from 0.6 to 8.0 psu (base case scenario) toward the onset of lagoon ice formation in late September.

5. Results

5.1. Stratigraphy, Temperature, and Porewater Chemistry

The RD borehole log showed silt in the upper 5.1 m of sediment overlying sands until 27.5 m (Figure 3). In the upper 0.7 m, the silt was clayey and exhibited plastic behavior. From 0.7 to 5.1 m, the silt was nonplastic, gray, and contained traces of fine sand. Ice was observed in the sediment between 4.8 and 8.3 m and as a thin lens at 15 m. The ground ice consisted of large transparent ice inclusions as large as 5.5 cm by 3.5 cm (Figure 3). The ice was bonded to the silt and visually represented 30% to 50% of the core by volume. The sands were fine-grained and gray, but a transition to coarse-grained sand with fine gravel occurred at a depth of 19.2 m.

The temperature cable data and freezing point temperatures (T_f) of the porewater from both the RD and UWITEC sediment cores are also shown in Figure 3. The freezing points were calculated from Equation 2 after converting electrical conductivity to molality using the TEOS-10 Thermodynamic Dynamic Equation of Seawater package in MATLAB (McDougall & Barker, 2011). The observed temperatures and

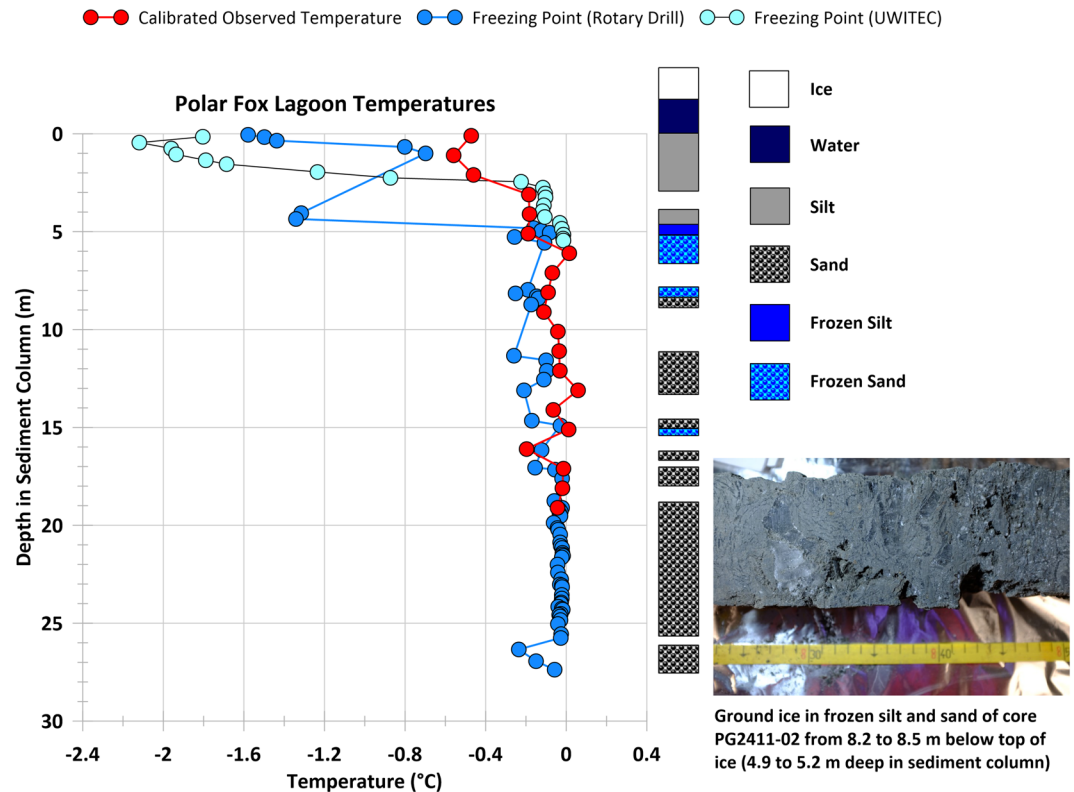


Figure 3. Borehole stratigraphy, observed temperatures, and the freezing points of thawed sediment porewater from Polar Fox Lagoon in April 2017. Gaps in the sediment log indicate core loss. An example of the ground ice structure observed in the ice-bearing permafrost is shown in the bottom right of the figure. The water depths for the RD and UWITEC boreholes were 3.3 and 3.1 m.

stratigraphic descriptions are both from the RD location. For the UWITEC core, the minimum T_f was -2.1°C at 0.5 m bsf, and for the RD, the minimum T_f was -1.6°C at the lagoon bed. In both cases, the T_f was well below the minimum observed temperature of -0.6°C at 1.1 m bsf. For the RD, there was a sharp increase in the T_f 4.8 m below the lagoon bed, which corresponded to the top of IBP. At a depth of 5.1 m, most T_f values were above the observed temperature. However, at the bottom of the IBP, the T_f was 0.1°C below the observed temperature. The UWITEC T_f increased from -2.1°C at 0.5 m below the surface to -0.1°C at 2.8 m. Below 2.1 m, the UWITEC T_f values were above the observed temperatures from the RD location. Since the UWITEC cannot penetrate bonded IBP, the sediment was likely deformable permafrost from 2.1 to 5.5 m. Most of the observed temperatures below the IBP were slightly cryotic and as low as -0.2°C . In all cases, the observed temperatures were equal to or above T_f except at 16 m. This occurred close to the thin ground ice lens observed at 15 m.

5.2. Seasonal Changes in Water Chemistry

The CTD casts showed seasonal and interannual variation in temperature and salinity. In April 2017, the minimum water temperature below the ice was -0.8°C compared to -2.4°C in April 2019 (Figure 2). The salinity in April 2017 was 13 psu compared to 44 psu in April 2019. The lagoon was significantly more saline than Tiksi Bay. At 200–400 m offshore of the Polar Fox channel, the salinity below the ice was approximately 4 psu in April 2019. During the summer of 2017, however, Polar Fox and Tiksi Bay showed very similar salinities. In Tiksi Bay, the salinity ranged from 0.6 to 0.8 psu, and in Polar Fox Lagoon, the salinity was fairly constant at 0.7 psu. The temperature of Tiksi Bay ranged from 6°C to 7°C and in Polar Fox Lagoon from 8.5°C to 9.5°C . We also investigated Northern Polar Fox Lake in April 2017. The lake was fresh (0.1 psu), suggesting no present connection with Polar Fox Lagoon.

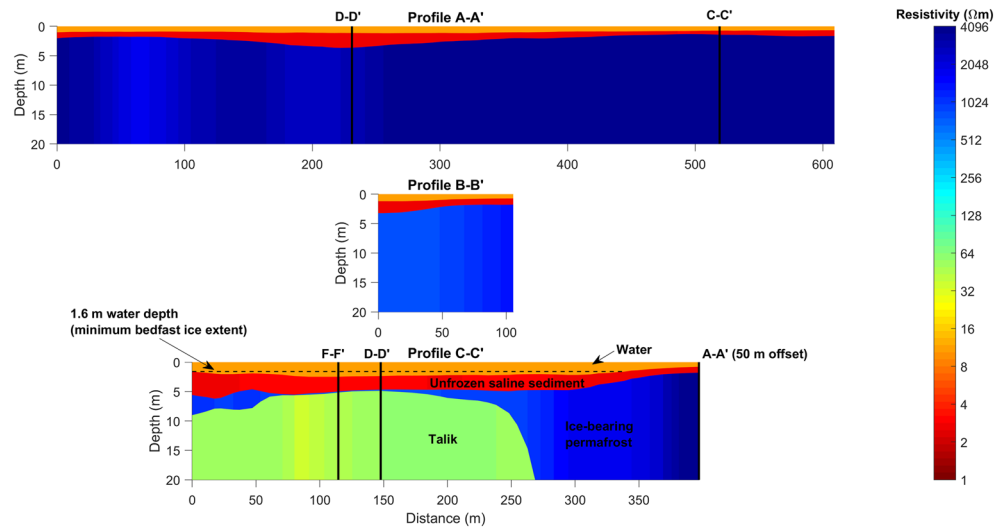


Figure 4. Laterally constrained layered inversions for profiles A-A', B-B', and C-C'. Refer to Figure 1c for start/end positions of the survey lines. Profile intersections are indicated by the black vertical lines.

5.3. Electrical Resistivity Surveys

To account for borehole stratigraphy, layered laterally constrained 1-D inversions (LCI) (Auken et al., 2005) were performed using Aarhus WorkbenchTM software. Four layers were selected to represent the stratigraphy observed in the borehole. The starting model resistivities for each unit were 10.4, 2.7, 1,000, and 50 Ωm with standard deviation factors of 1.01, 2.0, 4.0, and 2.0, respectively. While the water layer thickness was set by the echo soundings, the thicknesses of the remaining layers were left unconstrained. The resistivity of the saline layer was calculated using Archie's law (Loke, 2004), while adjusting the measured porewater resistivity for observed field temperatures following Hayashi (2004). We did not account for temperature changes from April (drilling campaign) to July (geoelectric surveys) in the near-surface sediment. A resistivity of 1,000 Ωm is typical for ice-bearing sand just below 0°C (R. Fortier et al., 1994), and 50 Ωm is reasonable for unfrozen saturated sand with brackish porewater. The T_f profiles shown in Figure 3 are indicative of an unfrozen saline layer above the IBP. Moderate standard deviation factors of 1.3 were used for the

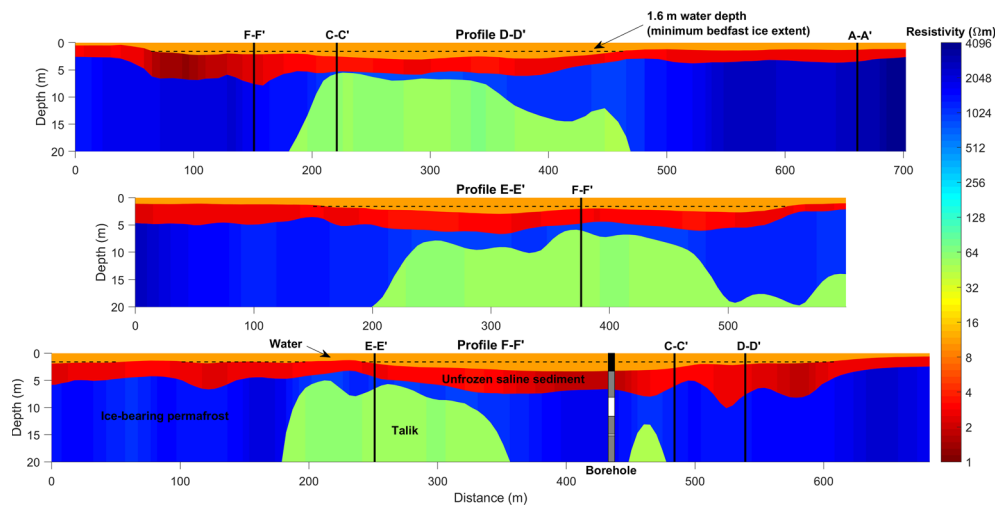


Figure 5. Laterally constrained layered inversions for profiles D-D', E-E', and F-F'. Refer to Figure 1c for start/end positions of the survey lines. Profile intersections are indicated by the black vertical lines. For the borehole, the black region is the water layer, the gray regions indicate unfrozen sediment, and the white regions indicate ice-bearing sediment.

Table 2
Resulting Boundary Condition Statistics for Polar Fox Lake to Lagoon Model Runs

Scenario	MABT (°C)	MABS (mol/m ³)	Max S (mol/m ³)	Max IT (m)	Min T_f (°C)
1. Base case	0.15	616	1,555	1.78	-2.89
2. Coarse sand	0.15	616	1,555	1.78	-2.89
3. Windswept	-1.26	1,377	3,920	2.28	-7.28
4. Snowpack	0.55	403	865	1.40	-1.61
5. Low salinity	0.41	469	1,197	1.80	-2.22
6. High salinity	-0.33	894	2,205	1.74	-4.09
7. Cool winter	0.00	660	1,686	1.83	-3.13
8. Warm winter	0.35	561	1,425	1.73	-2.65
9. Cool sea	0.02	616	1,555	1.78	-2.89
10. Warm sea	0.29	616	1,555	1.78	-2.89
11. Cool talik	0.15	616	1,555	1.78	-2.89
12. Rapid salt flow	0.15	616	1,555	1.78	-2.89
Field observations	—	850, 1,200 (RD, UWITEC)	1,473 (2019)	1.55–2.10 (2017)	-2.73 (2019)

Note. MABT = mean annual bottom water temperature; MABS = mean annual bottom water salinity; S = salinity; IT = lagoon ice thickness; Min = minimum; T_f = freezing point; and RD = rotary drill. The MABS is assumed to be similar to the near-surface porewater salinities from the sediment cores.

resistivity and thickness lateral constraints. Prior to running the inversion, we smoothed the apparent resistivity data with a 20 m mean filtering window. Upon data import, an assumed standard deviation of 5% was set for the apparent resistivity in the model residual calculations.

The inverted ERT profiles are shown in Figures 4 and 5. For each profile, the total data residual was less than 1.0. Generally, the thicknesses of the highly resistive IBP layer and the overlying conductive saline layer increased and decreased toward the shoreline, respectively. For profile A-A', which was parallel to and no further than 100 m from the shoreline, all water depths were less than 1.3 m. The average unfrozen conductive layer thickness was 1.2 m, and the mean resistivity was 2.7 Ω m (i.e., close to the starting model). However, the mean resistivity of the IBP was 4,200 Ω m, a fourfold increase from the starting model. In some cases, the IBP's resistivity exceeded 10,000 Ω m. For every sounding, the modeled thickness of the IBP exceeded the maximum focus depth (22.4 m) for the largest electrode separation (120 m). In profile B-B', all water depths were less than 1.3 m. The mean thickness of the conductive saline unit was 1.4 m with a mean resistivity of 2.7 Ω m, and the mean resistivity of the IBP was 990 Ω m.

Profiles C-C', D-D', and E-E' traversed both shallow and deep water depths that were characterized by bedfast ice and floating ice conditions in spring. In each profile, very sharp lateral transitions in IBP thickness were observed. In all cases, the thickness of IBP decreased from tens of meters to less than 5 m over 20 to 30 m distances toward the center of the lagoon. The thin IBP (≤ 5 m) was mostly observed below water depths greater than 1.6 m. Drawing from Profiles A-A' and B-B', it is reasonable to assume deep thermokarst lake talik refreezing from bedfast ice in areas where the water depth was less than 1.6 m (i.e., 75% of the lagoon). Since the 1.6 m water depth contour represents a minimum bedfast ice extent estimate, thick IBP was also observed at some water depths between 1.6 and 2.1 m toward the center of the lagoon.

Profile F-F' crossed the RD borehole at 430 m, which showed 4.8 m of saline unfrozen ground overlying a 3.5 m thick layer of IBP. The inverted thickness of the conductive saline layer at the borehole intersection was 3.3 m. However, the bottom of the IBP layer exceeded 20 m. Paradoxically, this occurred in a 3.1 m water depth where there was floating ice in spring. Approximately 30 m to the right of the borehole intersection, the inverted thicknesses of the conductive saline layer and IBP were 4.8 and 5.1 m, and thus comparable to the core results. Generally, the data set is robust, given that the inversion results were similar at the profile intersections. For example, at the F-F'/E-E' intersection, the thicknesses and resistivities of the conductive saline layer were 2.5 m and 2.8 Ω m for F-F' and 2.7 m and 2.9 Ω m for E-E'. The thicknesses and resistivities of the IBP were 2.1 m and 1,049 Ω m for F-F' and 1.4 m and 896 Ω m for E-E'. At the F-F'/D-D' intersection, the thicknesses and resistivities of the conductive saline layer were 5.6 m and 2.5 Ω m for F-F' and 5.5 m and 2.4 Ω m for D-D'. For both profiles, the bottom of the IBP exceeded 20 m. The one major exception to

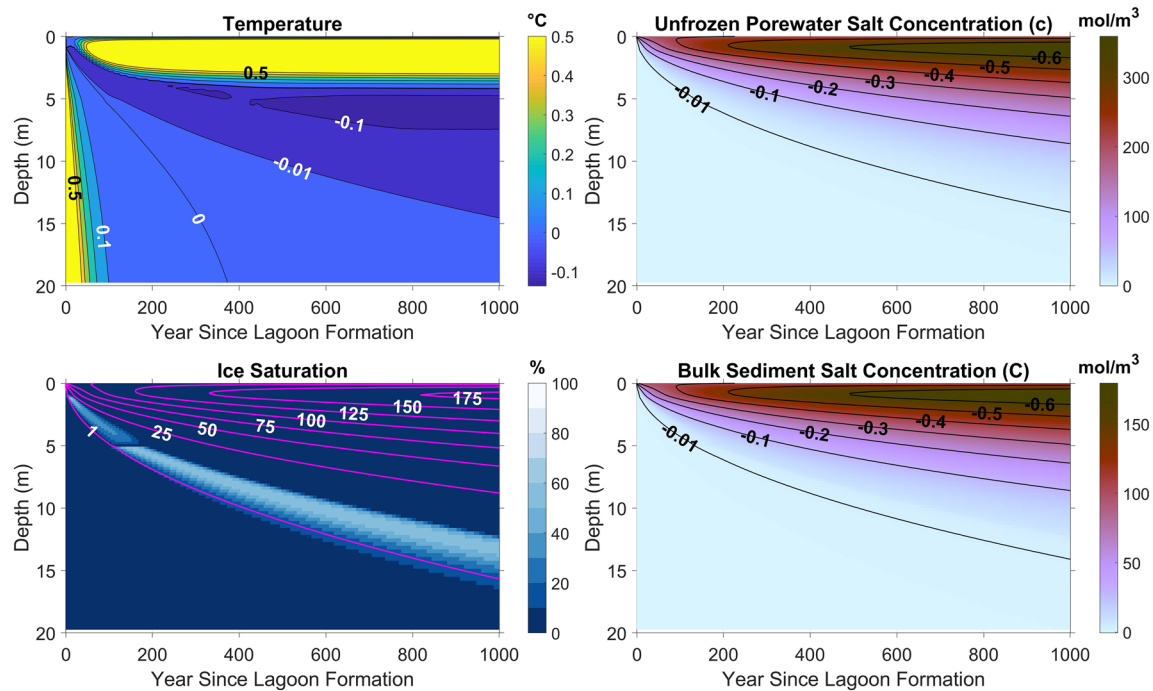


Figure 6. The evolution of temperature, ice saturation, and salt dynamics for Scenario 1 (base case). The annual model outputs at the end of September are shown. The bulk sediment salt concentration contours are superimposed on the ice saturation graph. The freezing point of liquid porewater contours are superimposed on the salt concentration graphs. The freezing characteristic curve of the sediment shifts from silt to sand at a depth of 5.1 m.

robustness was the C-C' and F-F' intersection close to the RD borehole. Here, the IBP thickness was 0.2 m for C-C' and greater than 14 m for F-F'. Therefore, 3-D geology effects on apparent resistivity are suspected. Further evidence for 3-D effects is that Profile F-F' shows thick IBP beneath water depths greater than 3 m, which contradicts the other profiles, as well as the borehole and thermal modeling results.

5.4. Heat and Salt Flow Modeling

The modeled talik depth after a thermokarst lake phase of 5,000 years was 107 m. After the lake to lagoon transition, the talik's response was highly sensitive to subtle changes in mean annual bottom water temperature and salinity. For the base case (Scenario 1), the mean annual bottom water temperature was 0.15°C. The resulting boundary condition statistics for all scenarios are presented in Table 2. Despite a positive mean bottom water temperature, a thin layer of IBP still developed (Figure 6). In this paper, IBP is defined as any sediment containing greater or equal to 10% ice saturation. For the first 200 years after lagoon formation, the thickness of the IBP gradually increased, but its average ice saturation decreased. Once the freezing front penetrated through the top of the sand unit at 5.1 m, the ice saturation increased to 50% to 60% because of the sand's steeper freezing characteristic curve. Compared to the RD borehole, which showed an IBP thickness of 3.5 m starting 4.8 m below the bed, the thickness of the modeled IBP was only 1.0 m when the depth to IBP was 4.8 m (170 years since lagoon formation). On the other hand, when the modeled thickness of IBP was 3.5 m, the top of IBP lay 10.5 m below the lagoon bed after 770 years. The maximum modeled IBP thickness after 1,000 years was 4.0 m. Nevertheless, the modeled stratigraphic sequence of saline unfrozen cryotic ground, a thin IBP layer, and unfrozen ground was comparable to the borehole. As the IBP thickened, the top of the newly formed IBP was degraded by salt diffusion (Figure 6). The sediment temperatures below the IBP were positive for the first 100 years of the lagoon. After this point, the 0°C isotherm deepened faster than the bottom of the IBP. When this occurred, the zone separating the bottom of the IBP from the 0°C isotherm was essentially isothermal and very close to 0°C. The bottom of the IBP did not follow the 0°C isotherm, because the freezing characteristic curve of the sediment allowed unfrozen water at temperatures slightly below 0°C.

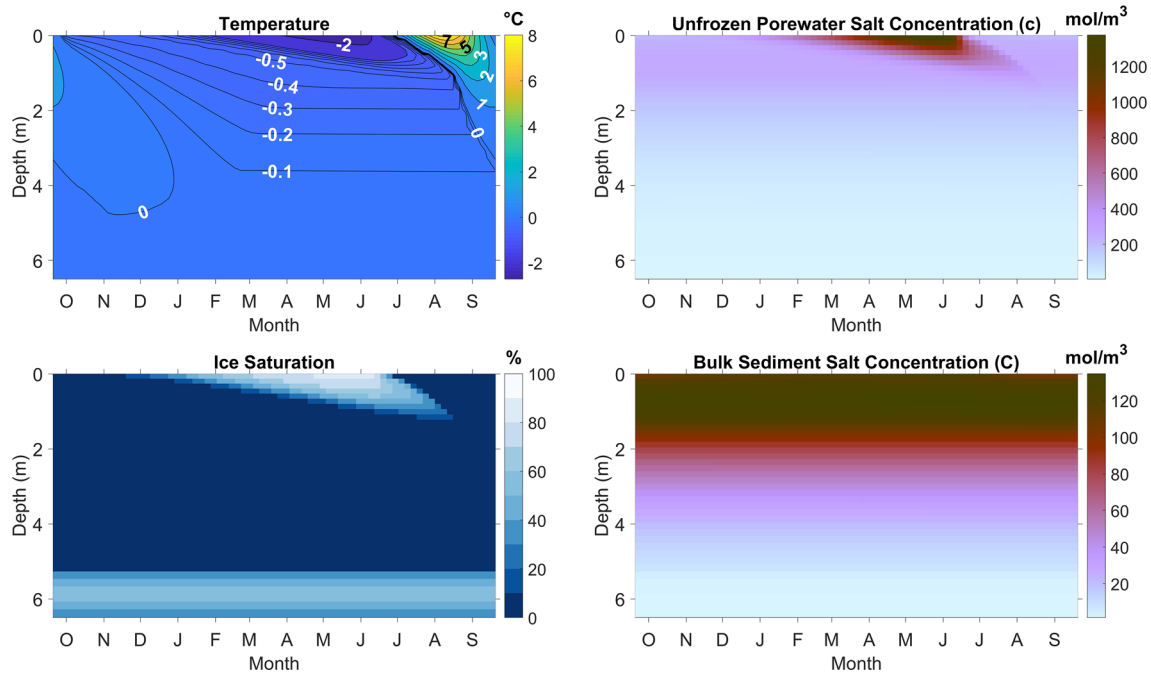


Figure 7. Annual dynamics 200 years after lagoon formation for Scenario 1 (base case).

The sediment temperatures below the IBP in the borehole were also slightly cryotic. The greatest difference between the borehole data and the modeled results was the porewater salinity. While the borehole showed maximum porewater salinities (in an unfrozen state) of 850 to 1,200 mol/m³, the maximum modeled porewater salinity in the near-surface sediment was approximately 350 mol/m³ for the base case (Scenario 1) in an unfrozen state. This occurred, despite the mean annual bottom water salinity of 616 mol/m³ as a boundary condition. However, over 1 year, the modeled porewater salinity increased as the temperature decreased and ice formed in the sediment (Figure 7). In this illustration, the depth to newly formed IBP was 5 m and

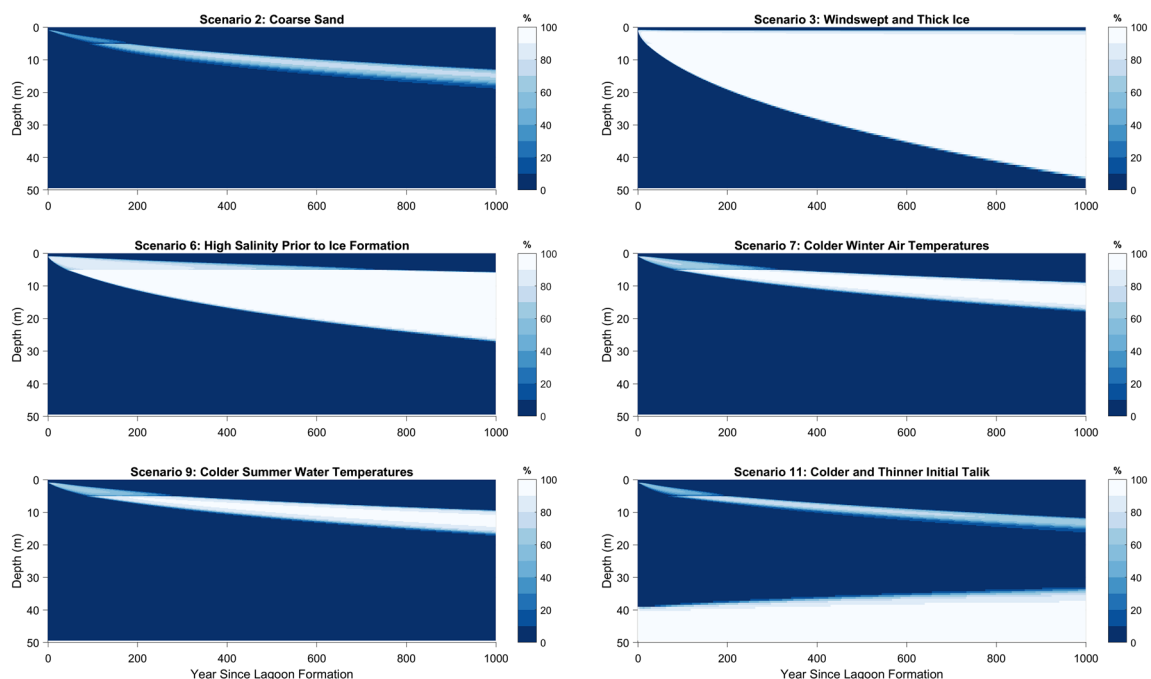


Figure 8. Annual outputs of ice saturation (late September) for thermokarst lake to lagoon transition models. The base case scenario and the models that did not produce IBP are not shown.

did not change throughout the year. Seasonal ice formation in the near-surface sediment started in December once the temperature dipped below T_f . The thickness of the seasonally frozen layer reached 1 m just before spring breakup and was completely thawed out by mid-August. The maximum ice saturation in the seasonally frozen layer was 80%. For the windswept (Scenario 3) and the high salinity (Scenario 6) models, the maximum porewater salt concentrations in an unfrozen state were 741 and 495 mol/m³, respectively.

Several other simulations reproduced an IBP thickness similar to the borehole results: Scenario 2 (coarse sand), Scenario 7 (cool winter), Scenario 9 (cool sea), and Scenario 11 (cool talik). After 1,000 years, the thicknesses of IBP were 5.6, 8.6, 7.4, and 4.0 m for the aforementioned scenarios, respectively (Figure 8). For Scenario 11, the initial talik thickness after lagoon formation was thinner, because the thermokarst lake phase was only 1,000 years. In this model, the depth to IBP at the base of the initial talik decreased from 40 to 35 m after 1,000 years following lagoon formation. The best fit with the borehole data was Scenario 9 (cool-sea). In this model, the peak summer water temperature was lowered by 1°C compared to the base case model. Here, the IBP thickness was 3.1 m when the top of the IBP was 4.8 m bsf. Scenario 6 (high salinity) and Scenario 3 (windswept) generated very thick IBP of 21 and 44 m depths after 1,000 years. However, the high-salinity model continued to degrade the top of IBP, while the windswept model did not degrade the top of IBP at all. For the high-salinity model (Scenario 6), an initial salinity of 12 psu instead of 8 psu resulted in a mean annual bottom water temperature of -0.33°C compared to 0.15°C . The maximum lagoon ice thickness, however, was minimally affected. For the windswept model (Scenario 3), which started with an initial salinity of 8 psu, the maximum lagoon ice thickness reached 2.3 m. Thus, the bottom water had a low mean annual temperature of -1.26°C . Any sensitivity analysis that raised the mean annual bottom water temperature above the base case value of 0.15°C resulted in no IBP formation. This included a 10 cm increase in max snow thickness, a 1°C air temperature increase during the lagoon ice formation season, a 1°C increase in maximum summer water temperature, and a 2 psu reduction in initial salinity prior to the onset of freezing. Increasing the salt diffusion coefficient by 1 order of magnitude also resulted in no IBP formation. For a numerical summary of IBP depths and thicknesses of the different model runs, refer to the supporting information (Table S1).

6. Discussion

6.1. Thermokarst Lake to Lagoon Transition

The original thermokarst lake basin likely developed during the early to mid-Holocene (Grosse et al., 2007). The modeled talik thickness after 5,000 years was 107 m, which is comparable to other studies. On the Alaskan coastal plain, thermokarst taliks over 90 m deep have been interpreted from TEM data (Creighton et al., 2018), and a talik 95 m deep was also interpreted from shallow seismics in the Lena Delta in Siberia (Schwamborn et al., 2002). In the initial phase of thermokarst development, the lake was completely isolated from Tiksi Bay (Figure 9a). Later, Polar Fox Lagoon experienced at least two drainage events, as evidenced by the paleo-channel in the northeast and the active southern channel. After the last drainage event, most of the lagoon became very shallow and connected to Tiksi Bay (Figure 9b). At this stage, the lagoon bottom was below sea level. Assuming today's bathymetry is similar to the water depths after drainage, at least 75% of the lagoon (water depth ≤ 1.6 m) was subject to bedfast ice after lagoon initiation. Where bedfast ice is present, IBP may form because of cold mean annual temperatures at the water/sediment interface. This is inferred from subsea permafrost studies in nearshore zones where ice-bearing sediment develops (Solomon et al., 2008). Bedfast ice may also slow talik development if it is only present for short durations (Roy-Leveillee & Burn, 2017). Hence, the transition from floating ice to bedfast ice can refreeze taliks. In saline waters, increased brine injection from bedfast ice might offset rapid cooling by lowering the freezing point of the porewater ahead of the freezing front (Overduin et al., 2012). This process has also been interpreted from a borehole transect in a hypersaline lagoon off the coast of Alaska for the geotechnical investigation of a pipeline (Miller, 2001). At this site, the hypersalinity promotes the chemical degradation of ice-rich permafrost, despite bedfast ice conditions. At Polar Fox Lagoon, the ERT surveys suggest deep talik refreezing in bedfast ice zones. Furthermore, the thickness of the saline sediments decreases toward the shoreline in shallower water, suggesting that salt diffusion operates more effectively toward the center of the lagoon where there is floating ice and warmer temperatures on the bed. For the lagoon center, we demonstrate that there are resistivity models containing a thin IBP layer that fit the observed apparent

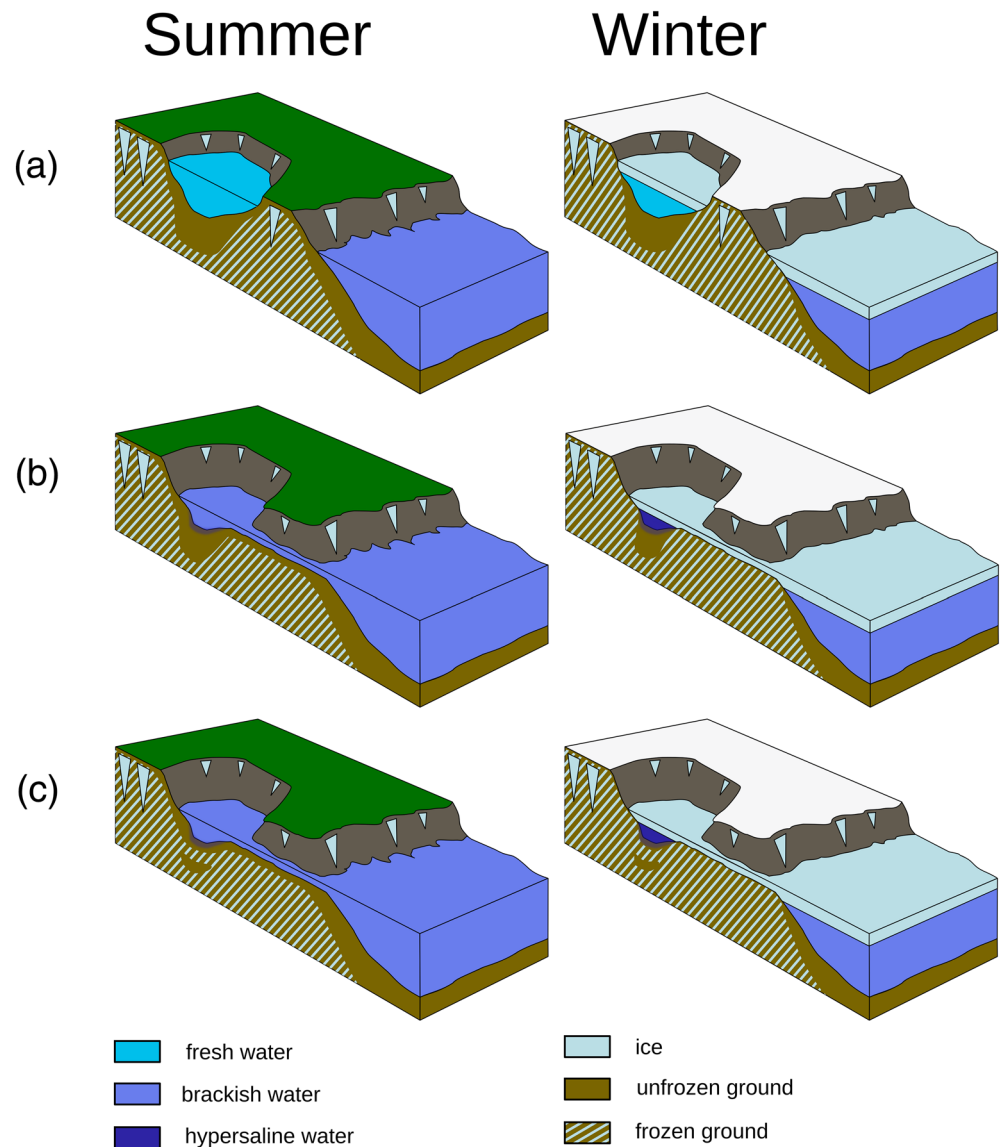


Figure 9. (a) Thermokarst lake phase and complete isolation from Tiksi Bay, (b) early lagoon phase and seasonal isolation from Tiksi Bay, and (c) late lagoon phase, seasonal isolation from Tiksi Bay, and partial talik refreezing.

resistivity data. The starting model was informed with a priori information from the borehole, which showed a thin IBP layer below saline unfrozen cryotic sediment. Thermal modeling shows that this IBP can form after lagoon formation.

The modeling of heat and salt diffusion suggests that the present-day boundary conditions are near the limit for what is needed to refreeze taliks in water with floating ice. Seasonal isolation from Tiksi Bay results in colder and more saline bottom water conditions under the ice cover in winter. Over time, this partially refreezes the underlying talik in floating ice zones (Figure 9c). Despite a positive mean bottom water temperature of 0.15°C in the base case model, IBP could still develop because of the thermal offset and seasonal variation in thermal properties of the seasonally frozen layer (Goodrich, 1982). However, the IBP was warm with a maximum ice saturation of only 60%. Therefore, the modeled pore space contained a mixture of ice and water, which is similar to the warm IBP conditions observed in the field. In this case, the frozen permafrost is ice-bearing and not ice-bonded and thus may still provide pathways for gas migration toward the surface. Considering the mean annual ground surface temperature warming observed in the region over the past few decades (Kneier et al., 2018), Polar Fox Lagoon was probably exposed to colder conditions at the

onset of the lake to lagoon transition. Not surprisingly, the cool winter (Scenario 7) and cool sea (Scenario 9) scenarios predicted an IBP evolution pattern that fits better with the borehole results. When the modeled depth to IBP was 4.8 m (like the borehole), the modeled IBP thicknesses were 4.6 and 3.4 m, compared to 1.0 m for the base case model. Recall that the IBP thickness observed from the borehole was 3.5 m. In both the cool sea and cool winter models, the peak water and mean annual air temperatures were only reduced by 1°C compared to the base case. Hence, the IBP formation rate is sensitive to climate change. More specifically, the IBP formation rate is very sensitive to lagoon ice thickness, because this controls the salt concentration in the water below the ice cover and thus the temperature. The 3-D concentration of salts into a shrinking liquid water volume as lagoon ice builds enhances the impact of a small change in ice thickness. This process explains why Polar Fox Lagoon was 10 times more saline than Tiksi Bay in April 2019. In the windswept model, the maximum lagoon ice thickness was 2.3 m. This resulted in a mean bottom water temperature of -1.3°C . In the windswept model, the IBP base was at 45 m after 1,000 years, but more interestingly, salt diffusion did not degrade the top of IBP at all. The colder the mean annual bottom water temperature, the less effective salt diffusion is at degrading newly formed IBP. This occurs, despite the higher salinity that accompanies colder water temperatures. For the high-salinity model, the mean annual bottom water temperature was -0.3°C , resulting in an IBP thickness of 21 m after 1,000 years. However, in this case, salt diffusion degraded the top of the IBP to 5 m. The low efficiency of salt diffusion for the windswept and high salinity models is partially caused by the freshwater influence of the Lena River. During the open water season when the seasonally frozen layer thaws, the salinity of the lagoon drops to 1 psu. During the lagoon ice season when salinities are high, salt diffusion is partially controlled by the amount of unfrozen water in the seasonally frozen layer. Once the porewater salinity of the seasonally frozen layer equals the bottom water salinity after partial freezing, the porewater salt concentration gradient is zero at the water/sediment interface, and any additional salt input from the water column stops.

Additional factors affecting the rate of IBP formation include the initial talik thickness and temperature, as well as the sediment porosity. However, the effects are minor compared to the impacts of air temperature, the lagoon's initial salinity, and snow.

Today, the Polar Fox Lagoon thermal regime is possibly in disequilibrium. The CTD data suggest that the boundary conditions shifted from IBP-thawing conditions in 2017 to IBP-formation conditions in 2019, because the water temperatures underneath the ice cover in April were -0.8°C and -2.4°C in both years, respectively. However, the maximum porewater salinities measured in the borehole are reflective of the long-term mean annual bottom water salinities if we assume molecular diffusion as the dominant mechanism for salt transport (Harrison & Osterkamp, 1982). In the UWITEC borehole, the maximum salinities occurred 0.5 m below the bed, which may be due to (i) the redistribution of salts upon seasonal freezing (Baker & Osterkamp, 1989), or (ii) the loss of salts to the water column through wave action, or (iii) upward diffusion during the open water season.

6.2. Mechanisms for Subaquatic IBP Formation

While the modeling suggests the thermokarst lake to lagoon transition occurred a few hundred years ago, the exact timings of the drainage events are unknown. More precise data on drained lake basin occurrence may be taken from radiocarbon dating in the peat on the high grounds of the land bridge separating the lagoon from Northern Polar Fox Lake. Even though the modeling shows how an unfrozen-frozen-unfrozen sediment sequence could develop, the formation of IBP may have occurred long after the formation of the lagoon. Although the RD borehole revealed a very sharp decrease in porewater salinity at the top of the IBP, the salinity gradually decreased from the bottom of the IBP to the base of the borehole. This gradual reduction in salinity with depth hints that salt diffusion might have preceded sediment freezing. Since regional air and permafrost ground temperatures have warmed over the past decades to centuries (Kneier et al., 2018), what could have caused the lagoon's upper boundary conditions to cool after its formation? One possible explanation is that the continued infilling of sediment resulted in a shallower lagoon. In floating ice areas, this serves to concentrate salt from seasonal brine expulsion into a smaller liquid water volume, thus creating colder conditions needed to refreeze taliks. Interstitial water motion may also contribute to IBP formation by freshening saline sediments and increasing the freezing point of the porewater (Frederick & Buffett, 2015). While IBP formation can be explained without water movement, porewater freshening might be responsible for the thin ice lens and slight drop in temperature observed at a depth of 15 m in the

borehole. Since the land bridge between Northern Polar Fox Lake and Polar Fox Lagoon has likely refrozen tens of meters since the onset of subaerial exposure, we assume that there is no significant groundwater flow and heat advection in this area.

Alternative theories of IBP formation include (i) seasonal freezing, (ii) changes in sea level and salinity, and (iii) subaerial exposure in between the thermokarst lake and lagoon phases.

- i. Seasonal freezing at a depth of 5 m is possible, provided that the negative temperature seawater is warmer than the freezing point of the near-surface sediments (0–5 m). In this situation, no energy is used for the phase change of water, so seasonal freezing could occur at a depth of 5 m. However, the thickness of ice-bearing sediment in the borehole was 3.5 m, and this is too thick for seasonal freezing in this setting. If seasonal freezing below the seabed occurs, the modeling suggests that 1 m is reasonable (Figure 7). Bogorodskii et al. (2018) modeled a 0.5 m thick seasonally frozen layer for a 3 m water depth with floating ice in Tiksi Bay, and field observations from Osterkamp et al. (1989) indicate that a seasonally frozen layer can develop under floating ice in Prudhoe Bay, Alaska.
- ii. Any sea level rise over the past few thousand years would have warmed the lagoon through deepening of the water column (i.e., less concentrated salts after sea ice formation). In addition, the Lena River has been increasing in discharge over the past several decades (Fedorova et al., 2015), and the modeling shows that a lower salinity at the onset of lagoon ice formation increases the mean annual bottom water temperature.
- iii. Schirrmeister et al. (2018) show that drained thermokarst lake basins may undergo a period of subaerial exposure before becoming a lagoon. This could certainly refreeze taliks very quickly, as much as 53 m in 157 years (Ling & Zhang, 2004). However, we suggest that the Polar Fox Lagoon did not experience a subaerial phase. The first insight into this is that the seafloor in the center of the lagoon is below sea level and that the most significant drainage channel connects to Tiksi Bay. The RD borehole did not reach the ice-bonded permafrost table, and since the base of the Yedoma Ice Complex is as low as 15 m below sea level (Grigoriev, 1993; Grosse et al., 2007; Shakhova et al., 2017), all the near-surface massive ground ice could have melted prior to lagoon formation. The second hint is that the IBP is very thin, thus implying very slow refreezing. If the lagoon was subaerially exposed for even just a few decades to a century, the newly formed IBP would be at least tens of meters thick. For example, even the windswept model (mean annual bottom water temperature of only -1.3°C) resulted in 20 m of refrozen talik in just 200 years. Lastly, the ice structure itself is not characteristic of subaerial exposure. After lake drainage, one could expect irregular-reticulate cryostructures to form in refreezing heterogeneous sediments (French & Shur, 2010). Furthermore, although slow refreezing is prerequisite for thick ice lenses, temperatures just below the freezing point may not produce enough cryosuction to migrate water up to the freezing front (Williams & Smith, 1991).

6.3. The Future of Polar Fox Lagoon

The current trends in lake ice thinning (Arp et al., 2012), warming Siberian shelf waters (Dmitrenko et al., 2011), and a longer open water season (Günther et al., 2015) all suggest that Polar Fox Lagoon will not be able to support its newly formed IBP over the next several decades. In fact, it may already be degrading. As the modeling shows, simply increasing the mean annual air temperature or peak summer water temperature by 1°C would lead to thawing of the IBP that had formed in the talik. Increasing winter snowfall could also thaw the IBP. Even if the IBP is preserved after the lagoon is encroached by the sea, the warm coastal waters will thaw out the newly formed IBP. After thawing, the absence of the IBP layer might only be temporary. As coastal erosion continues, the thawed out IBP layer will ultimately be exposed to seawater with negative mean annual bottom water temperatures. At this point, the IBP may return. For lagoon to sea simulations, refer to the supporting information (Figure S1). For the IBP to return, it is assumed that seafloor erosion does not remove the fine-grained sediment acting as a barrier to convective processes for the rapid transport of salt. Even if diffusion is the sole mechanism for salt transport, the frozen cap could ultimately disappear because the lower IBP boundary is limited by the geothermal heat flux. This may allow salt diffusion to catch up and finally overtake the freezing front, particularly in the upper 30 m of the sediment column where empirical models have shown diffusion to be effective for salt transport (Golubeva et al., 2018).

6.4. Implications for Effective Bulk Gas Diffusivity of Thawing Subaquatic Permafrost

Salt diffusion into the sediment brings sulfate to the freezing front, where anaerobic methane oxidation may then occur (Overduin et al., 2015; Winkel et al., 2018) and thus limit its release to the water column. If no IBP forms under floating ice conditions after lagoon formation, then the talik interior of the partially refrozen thermokarst lake talik beneath the bedfast ice zone may serve as a gas migration pathway for methane from deep subaquatic permafrost thawing or production within unfrozen sediment itself. However, if IBP forms beneath floating ice conditions, then the lagoon could temporarily become an impermeable barrier to gas flow below the IBP. The ice saturation within the IBP is critical, because poorly bonded IBP is permeable to gas flow (Chuvilin et al., 2016). Since the IBP deepens and thickens as the lagoon ages, some methane may get trapped in the newly formed frozen sediment. The release of methane from the newly formed IBP's chemical degradation to an increasingly thick and saline unfrozen sediment column should be slow over time. In the case that fresh porewater underlies the IBP, the anaerobic oxidation of methane in sediment can still occur for sediment temperatures close to 0°C (Winkel et al., 2019). Most of the gas that remains entrapped below the IBP could be released once the lagoon is exposed to warmer water temperatures after sufficient coastal erosion. Provided the right boundary conditions, lagoons may mitigate the release of methane to the water column and atmosphere in between the thermokarst lake and offshore phases of subaquatic talik and IBP development.

6.5. Limitations of Modeling Framework

The modeling successfully showed how IBP could simultaneously form and degrade following a talik's submergence in seawater. However, the modeled talik response is highly sensitive to bottom water temperature and salinity regimes, which may significantly influence model output and interpretation. An additional drawback of the modeling work was the inability to reproduce the porewater salinities measured from the borehole samples. The most likely explanation for the discrepancy is the simplistic ice growth and brine rejection calculations. The model ignores stratification in the water column and the possibility of T_f being lower than T_b . The latter may also be affected by solar heating through the ice cover, especially in spring (Boike et al., 2015). The higher the T_f/T_b ratio, the greater the salt diffusion (Harrison & Osterkamp, 1978). Since T_b is equal to T_f , the diffusion of salt during the sea ice season is controlled by the freezing characteristic curve of the sediment and the amount of unfrozen water in the seasonally frozen layer. More detailed models should consider an ice growth model for brine rejection (Cox & Weeks, 1983) in combination with an energy balance model similar to CryoGrid3 for thermokarst lakes (Langer et al., 2016; Westermann et al., 2016).

6.6. Electrical Resistivity Surveys

The inversions suggest that there are models containing a high-resistivity layer (greater than 1,000 Ωm) beneath the conductive saline layer that fit the observed apparent resistivity data within an acceptable misfit. Since the water resistivity and the porewater resistivity of the unfrozen saline sediment were measured, a reasonable starting model for the LCI was developed. The resistivity, thickness, and depth to IBP were then inverted for all geoelectric profiles. In Figure 4, the resistivity of thick ice-bearing material approaches 5,000 Ωm close to the shoreline and is closer to 1,000 Ωm toward the center of the lagoon where it is thin. In frozen ground, subtle changes in unfrozen water content may affect the apparent resistivity (Oldenborger & LeBlanc, 2018). In the center of the lagoon, the mapping of the thin IBP is facilitated by a few layered inversion scheme with well-constrained water and conductive saline units in the starting model. If a 2-D minimum structure model or L1-norm robust inversion scheme is used, then the thin IBP layer can be smeared out in the inversion. Auken et al. (2005) show the challenges of recognizing layer boundaries for 2-D minimum structure models compared to LCI, while Auken and Christiansen (2004) show how LCI models are improved with a priori depth information. As shown in Profile D-D' (Figure 5), the thickness of the IBP was poorly resolved and only tens of centimeters thick in some areas. The profile intersection points allow us to test the inversions, because single profiles represent independent data sets. The intersection points show similar resistivities and layer thicknesses (Figures 4 and 5), except for the C-C' and F-F' crossing close to the RD borehole. We speculate this is because the water depths measured with the echo sounder were not representative of the mean water depth affecting the measured apparent resistivities. While a 3-D inversion could help solve these issues, we opted for the LCI method to constrain the inversion with a priori borehole data. The model layer thicknesses and resistivities for the profile intersections are shown in the supporting information (Figures S2 and S3).

7. Conclusions

Observational data from electrical resistivity surveys, water column temperature and salinity, and sediment coring showed that a thermokarst lake talik, once inundated with seawater, may begin to freeze under bedfast and floating ice conditions. The inundation by seawater provides salt, which is concentrated during winter ice formation. This leads to the development of a saline sediment layer, but also to cold (cryotic) bottom water temperatures. While the salt diffuses into the sediment, potentially lowering the freezing point and thawing permafrost, the colder bottom temperatures propagate into the talik and can refreeze the sediment ahead of the salt front. Modeling shows that this system is close to equilibrium and that small changes in system components that affect permafrost boundary conditions (e.g., snow and ice thickness and seawater salinity) can switch IBP formation on or off. At the lagoon that forms the focus of this study, freezing below bedfast ice creates an annulus of permafrost surrounding the deeper center of the lagoon, where brines created by salt rejection allow for subzero water temperatures and salt diffusion into the sediment. We show that, at this location, this has led to the creation of an ice-bearing layer 4.8 to 8.3 m below the lagoon floor, effectively capping the talik below. Our study provides evidence of the possibility that IBP may form under subaquatic conditions and that not all subsea IBP in the Arctic is inundated terrestrial permafrost.

Data Availability Statement

Field and modeling data are available on PANGAEA (at <https://doi.pangaea.de/10.1594/PANGAEA.907479>).

References

- Angelopoulos, M., Westermann, S., Overduin, P. P., Faguet, A., Olenchenko, V., Grosse, G., & Grigoriev, M. N. (2019). Heat and salt flow in subsea permafrost modeled with CryoGRID2. *Journal of Geophysical Research: Earth Surface*, *124*, 920–937. <https://doi.org/10.1029/2018JF004823>
- Arp, C. D., Jones, B. M., Lu, Z., & Whitman, M. S. (2012). Shifting balance of thermokarst lake ice regimes across the Arctic Coastal Plain of northern Alaska. *Geophysical Research Letters*, *39*, L16503. <https://doi.org/10.1029/2012GL052518>
- Atkins, P. W., De Paula, J., & Keeler, J. (2018). *Atkins' physical chemistry*. Oxford: Oxford University Press.
- Auken, E., & Christiansen, A. V. (2004). Layered and laterally constrained 2D inversion of resistivity data. *Geophysics*, *69*(3), 752–761. <https://doi.org/10.1190/1.1759461>
- Auken, E., Christiansen, A. V., Jacobsen, B. H., Foged, N., & Sørensen, K. I. (2005). Piecewise 1D laterally constrained inversion of resistivity data. *Geophysical Prospecting*, *53*(4), 497–506. <https://doi.org/10.1111/j.1365-2478.2005.00486.x>
- Baker, G. C., & Osterkamp, T. E. (1989). Salt redistribution during freezing of saline sand columns at constant rates. *Water Resources Research*, *25*(8), 1825–1831. <https://doi.org/10.1029/WR025i008p01825>
- Bauch, H. A., Kassens, H., Naidina, O. D., Kunz-Pirrung, M., & Thiede, J. (2001). Composition and flux of Holocene sediments on the eastern Laptev Sea shelf, Arctic Siberia. *Quaternary Research*, *55*(3), 344–351. <https://doi.org/10.1006/qres.2000.2223>
- Biskaborn, B. K., Herzschuh, U., Bolshiyakov, D., Schwamborn, G., & Diekmann, B. (2013). Thermokarst processes and depositional events in a tundra lake, northeastern Siberia. *Permafrost and Periglacial Processes*, *24*(3), 160–174. <https://doi.org/10.1002/ppp.1769>
- Biskaborn, B. K., Smith, S. L., Noetzi, J., Matthes, H., Vieira, G., Streletskiy, D. A., et al. (2019). Permafrost is warming at a global scale. *Nature Communications*, *10*(1), 264. <https://doi.org/10.1038/s41467-018-08240-4>
- Bogorodskii, P. V., Pnyushkov, A. V., & Kustov, V. Y. (2018). Seasonal freezing of a subwater ground layer at the Laptev Sea shelf, *The Ocean in Motion* (pp. 611–625). Cham: Springer. https://doi.org/10.1007/978-3-319-71934-4_39
- Boike, J., Georgi, C., Kirilov, G., Muster, S., Abramova, K., Fedorova, I., et al. (2015). Thermal processes of thermokarst lakes in the continuous permafrost zone of northern Siberia—Observations and modeling (Lena River Delta, Siberia). *Biogeosciences*, *12*(20), 5941. <https://doi.org/10.5194/bg-12-5941-2015>
- Cheverev, V. G., Vidyapin, I. Y., & Tumskey, V. E. (2007). Bykovsky peninsula, thermokarst lagoons, ground composition and properties. *Kriosfera Zemli*, *11*(3), 44–50.
- Chuvilin, E. M., Ekimova, V., Bukhanov, B., Grebenkin, S., Shakhova, N., & Semiletov, I. (2019). Role of salt migration in destabilization of intra permafrost hydrates in the Arctic Shelf: Experimental modeling. *Geosciences*, *9*(4), 188. <https://doi.org/10.3390/geosciences9040188>
- Chuvilin, E. M., Grebenkin, S. I., & Sacleux, M. (2016). Influence of moisture content on permeability of frozen and unfrozen soils. *Kriosfera Zemli*, *20*, 66–72.
- Cosenza, P., Guerin, R., & Tabbagh, A. (2003). Relationship between thermal conductivity and water content of soils using numerical modelling. *European Journal of Soil Science*, *54*(3), 581–588. <https://doi.org/10.1046/j.1365-2389.2003.00539.x>
- Cox, G. F. N., & Weeks, W. F. (1983). Equations for determining the gas and brine volumes in sea-ice samples. *Journal of Glaciology*, *29*(102), 306–316. <https://doi.org/10.3189/S0022143000008364>
- Creighton, A. L., Parsekian, A. D., Angelopoulos, M., Jones, B. M., Bondurant, A., Engram, M., et al. (2018). Transient electromagnetic surveys for the determination of talik depth and geometry beneath thermokarst lakes. *Journal of Geophysical Research: Solid Earth*, *123*, 9310–9323. <https://doi.org/10.1029/2018JB016121>
- Dall'Amico, M., Endrizzi, S., Gruber, S., & Rigon, R. (2011). A robust and energy-conserving model of freezing variably-saturated soil. *The Cryosphere*, *5*(2), 469. <https://doi.org/10.5194/tc-5-469-2011>
- Dmitrenko, I. A., Kirillov, S. A., Tremblay, L. B., Kassens, H., Anisimov, O. A., Lavrov, S. A., et al. (2011). Recent changes in shelf hydrography in the Siberian Arctic: Potential for subsea permafrost instability. *Journal of Geophysical Research*, *116*, C10027. <https://doi.org/10.1029/2011JC007218>

Acknowledgments

The fieldwork was funded by the Alfred Wegener Institute, Helmholtz Centre for Polar and Marine Research (AWI), the German Research Centre for Geosciences (GFZ), and the PETA-CARB project (ERC 338335). Logistical support was provided by Hydrobase in Tiksi and the Lena Delta Reserve. Submarine permafrost studies were supported by Russian Foundation for Basic Research (RFBR/RFFI) Grant 18-05-70091. Additional support was provided by the European Union's Horizon 2020 Research and Innovation Programme under Grant Agreement 773421 (Nunataryuk). We are very thankful to Bennet Juhls (Freie Universität Berlin), who was part of the summer expedition and provided invaluable scientific and technical support. In addition, we are grateful to Frederieke Miesner (Alfred Wegener Institute) for helping with the 3-D figure presented in the paper. The 2019 conductivity, temperature, and depth (CTD) data were collected as part of the CACOON project (NERC-BMBF Grant, project CACOON, Grant 03F0806A), so we thank Matthias Fuchs (Alfred Wegener Institute) for his fieldwork support. Additional support was provided by Frank Günther (University of Potsdam), who processed the WorldView-3 imagery shown in this paper. Open access funding enabled and organized by Projekt DEAL.

- Dugan, H. A., & Lamoureux, S. F. (2011). The chemical development of a hypersaline coastal basin in the High Arctic. *Limnology and Oceanography*, 56(2), 495–507. <https://doi.org/10.4319/lo.2011.56.2.0495>
- Dutilleul, P., Haltigin, T. W., & Pollard, W. H. (2009). Analysis of polygonal terrain landforms on Earth and Mars through spatial point patterns. *Environmetrics: The Official Journal of the International Environmetrics Society*, 20(2), 206–220. <https://doi.org/10.1002/env.924>
- Fedorova, I., Chetverova, A., Bolshiyarov, D., Makarov, A., Boike, J., Heim, B., et al. (2015). Lena Delta hydrology and geochemistry: Long-term hydrological data and recent field observations. *Biogeosciences*, 12(2), 345–363. <https://doi.org/10.5194/bg-12-345-2015>
- Fortier, R., Allard, M., & Seguin, M. K. (1994). Effect of physical properties of frozen ground on electrical resistivity logging. *Cold Regions Science and Technology*, 22(4), 361–384. [https://doi.org/10.1016/0165-232X\(94\)90021-3](https://doi.org/10.1016/0165-232X(94)90021-3)
- Fortier, D., Allard, M., & Shur, Y. (2007). Observation of rapid drainage system development by thermal erosion of ice wedges on Bylot Island, Canadian Arctic Archipelago. *Permafrost and Periglacial Processes*, 18(3), 229–243. <https://doi.org/10.1002/ppp.595>
- Frederick, J. M., & Buffett, B. A. (2014). Taliks in relict submarine permafrost and methane hydrate deposits: Pathways for gas escape under present and future conditions. *Journal of Geophysical Research: Earth Surface*, 119, 106–122. <https://doi.org/10.1002/2013JF002987>
- Frederick, J. M., & Buffett, B. A. (2015). Effects of submarine groundwater discharge on the present-day extent of relict submarine permafrost and gas hydrate stability on the Beaufort Sea continental shelf. *Journal of Geophysical Research: Earth Surface*, 120, 417–432. <https://doi.org/10.1002/2014JF003349>
- French, H., & Shur, Y. (2010). The principles of cryostratigraphy. *Earth-Science Reviews*, 101(3–4), 190–206. <https://doi.org/10.1016/j.earscirev.2010.04.002>
- Günther, F., Overduin, P. P., Yakshina, I. A., Opel, T., Baranskaya, A. V., & Grigoriev, M. N. (2015). Observing Muostakh disappear: Permafrost thaw subsidence and erosion of a ground-ice-rich island in response to Arctic summer warming and sea ice reduction. *The Cryosphere*, 9(1), 151–178. <https://doi.org/10.5194/tc-9-151-2015>
- Golubeva, E., Platov, G., Malakhova, V., Kraineva, M., & Iakshina, D. (2018). Modelling the long-term and inter-annual variability in the Laptev Sea hydrography and subsea permafrost state. *Polarforschung*, 87(2), 195–210. <https://doi.org/10.2312/polarforschung.87.2.195>
- Goodrich, L. E. (1982). The influence of snow cover on the ground thermal regime. *Canadian Geotechnical Journal*, 19(4), 421–432. <https://doi.org/10.1139/t82-047>
- Grigoriev, M. N. (1993). Cryomorphogenesis of the Lena Delta mouth area. Permafrost Institute, Academy of Science USSR, Siberian Department, Yakutsk, 1–176.
- Grigoriev, M. N. (2008). Kriomorphogenez i litodinamika pribrezhno-shelfovoi zony morei vostochnoi sibirii (Cryomorphogenesis and lithodynamics of the East Siberian near-shore shelf zone) (Habilitation thesis), Melnikov Permafrost Institute, Russian Academy of Sciences, Siberian Branch, Yakutsk.
- Grosse, G., Schirrmeister, L., Siegert, C., Kunitsky, V. V., Slagoda, E. A., Andreev, A. A., & Dereviagin, A. Y. (2007). Geological and geomorphological evolution of a sedimentary periglacial landscape in northeast Siberia during the Late Quaternary. *Geomorphology*, 86(1), 25–51. <https://doi.org/10.1016/j.geomorph.2006.08.005>
- Grotheer, H., Meyer, V., Riedel, T., Pfalz, G., Mathieu, L., Heftner, J., et al. (2020). Burial and origin of permafrost derived carbon in the nearshore zone of the southern Canadian Beaufort Sea. *Geophysical Research Letters*, 47, e2019GL085897. <https://doi.org/10.1029/2019GL085897>
- Harris, C. M., McClelland, J. W., Connelly, T. L., Crump, B. C., & Dunton, K. H. (2017). Salinity and temperature regimes in eastern Alaskan Beaufort Sea lagoons in relation to source water contributions. *Estuaries and Coasts*, 40(1), 50–62. <https://doi.org/10.1007/s12237-016-0123-z>
- Harris, C. M., McTigue, N. D., McClelland, J. W., & Dunton, K. H. (2018). Do High Arctic coastal food webs rely on a terrestrial carbon subsidy? *Food Webs*, 15, e00081. <https://doi.org/10.1016/j.fooweb.2018.e00081>
- Harrison, W. D., & Osterkamp, T. E. (1978). Heat and mass transport processes in subsea permafrost 1. An analysis of molecular diffusion and its consequences. *Journal of Geophysical Research*, 83(C9), 4707–4712. <https://doi.org/10.1029/JC083iC09p04707>
- Harrison, W. D., & Osterkamp, T. E. (1982). Measurements of the electrical conductivity of interstitial water in subsea permafrost. In *Proceedings of the Fourth Canadian Permafrost Conference* (pp. 229–237). Ottawa, Canada: National Research Council of Canada.
- Hayashi, M. (2004). Temperature-electrical conductivity relation of water for environmental monitoring and geophysical data inversion. *Environmental Monitoring and Assessment*, 96(1-3), 119–128. <https://doi.org/10.1023/B:EMAS.0000031719.83065.68>
- Jenrich, M. (2020). Thermokarst lagoons - Carbon pools and panarctic distribution. Masters thesis, University of Potsdam, Potsdam.
- Juhls, B., Overduin, P. P., Hölemann, J., Hieronymi, M., Matsuoka, A., Heim, B., & Fischer, J. (2019). Dissolved organic matter at the fluvial-marine transition in the Laptev Sea using in situ data and ocean colour remote sensing. *Biogeosciences*, 16, 2693–2713. <https://doi.org/10.5194/bg-16-2693-2019>
- Kaplina, T. N. (2009). Alas complex of Northern Yakutia. *Earth's Cryosphere*, 13(4), 3–17.
- Kasprzak, M., Strzelecki, M. C., Traczyk, A., Kondracka, M., Lim, M., & Migala, K. (2017). On the potential for a bottom active layer below coastal permafrost: The impact of seawater on permafrost degradation imaged by electrical resistivity tomography (Hornsund, SW Spitsbergen). *Geomorphology*, 293, 347–359. <https://doi.org/10.1016/j.geomorph.2016.06.013>
- Kneier, F., Overduin, P. P., Langer, M., Boike, J., & Grigoriev, M. N. (2018). Borehole temperature reconstructions reveal differences in past surface temperature trends for the permafrost in the Laptev Sea region, Russian Arctic. *Arktos*, 4(1), 7. <https://doi.org/10.1007/s41063-018-0041-3>
- Lachenbruch, A. H., Sass, J. H., Marshall, B. V., & Moses Jr, T. H. (1982). Permafrost, heat flow, and the geothermal regime at Prudhoe Bay, Alaska. *Journal of Geophysical Research*, 87(B11), 9301–9316. <https://doi.org/10.1029/JB087iB11p09301>
- Langer, M., Westermann, S., Boike, J., Kirillin, G., Grosse, G., Peng, S., & Krinner, G. (2016). Rapid degradation of permafrost underneath waterbodies in tundra landscapes—Toward a representation of thermokarst in land surface models. *Journal of Geophysical Research: Earth Surface*, 121, 2446–2470. <https://doi.org/10.1002/2016JF003956>
- Lantuit, H., Atkinson, D., Overduin, P. P., Grigoriev, M., Rachold, V., Grosse, G., & Hubberten, H.-W. (2011). Coastal erosion dynamics on the permafrost-dominated Bykovsky Peninsula, North Siberia, 1951–2006. *Polar Research*, 30(1), 7341. <https://doi.org/10.3402/polar.v30i0.7341>
- Lee, M. W. (2005). Well log analysis to assist the interpretation of 3d seismic data at Milne Point, North Slope of Alaska, scientific investigations report 2005–5048. <http://pubs.usgs.gov/sir/2005/5048/>
- Leppäranta, M. (1993). A review of analytical models of sea-ice growth. *Atmosphere-Ocean*, 31(1), 123–138. <https://doi.org/10.1080/07055900.1993.9649465>
- Ling, F., & Zhang, T. (2004). Modeling study of talik freeze-up and permafrost response under drained thaw lakes on the Alaskan Arctic Coastal Plain. *Journal of Geophysical Research*, 109, D01111. <https://doi.org/10.1029/2003JD003886>

- Loke, M. H. (2004). Tutorial: 2-D and 3-D electrical imaging surveys.
- Malakhova, V. V. (2016). On the thermal influence of thermokarst lakes on the subsea permafrost evolution. In *22nd International Symposium on Atmospheric and Ocean Optics: Atmospheric Physics*, 10035, 100355U. <https://doi.org/10.1117/12.2248714>
- Matthews, J. B., & Stringer, W. J. (1984). Spring breakup and flushing of an Arctic lagoon estuary. *Journal of Geophysical Research*, *89*(C2), 2073–2079. <https://doi.org/10.1029/JC089iC02p02073>
- McDougall, T. J., & Barker, P. M. (2011). Getting started with TEOS-10 and the Gibbs Seawater (GSW) oceanographic toolbox. *SCOR/IAPSO WG*, *127*, 1–28.
- Miller, D. L. (2001). Hypersaline permafrost under a lagoon of the Arctic Ocean. In *Proceedings of the international conference on port and ocean engineering under arctic conditions*. <https://trid.trb.org/view/1395175>
- Nicolosky, D. J., Romanovsky, V. E., Romanovskii, N. N., Kholodov, A. L., Shakhova, N. E., & Semiletov, I. P. (2012). Modeling sub-sea permafrost in the East Siberian Arctic Shelf: The Laptev Sea region. *Journal of Geophysical Research*, *117*, F03028. <https://doi.org/10.1029/2012JF002358>
- Nicolosky, D. J., & Shakhova, N. (2010). Modeling sub-sea permafrost in the East Siberian Arctic Shelf: The Dmitry Laptev Strait. *Environmental Research Letters*, *5*(1), 015006. <https://doi.org/10.1088/1748-9326/5/1/015006>
- Oldenborger, G. A., & LeBlanc, A.-M. (2018). Monitoring changes in unfrozen water content with electrical resistivity surveys in cold continuous permafrost. *Geophysical Journal International*, *215*(2), 965–977. <https://doi.org/10.1093/gji/ggy321>
- Osterkamp, T. E. (2001). *Sub-sea permafrost, Elements of Physical Oceanography: A Derivative of the Encyclopedia of Ocean Sciences*, 2 (pp. 2902–2912).
- Osterkamp, T. E., Baker, G. C., Harrison, W. D., & Matava, T. (1989). Characteristics of the active layer and shallow subsea permafrost. *Journal of Geophysical Research*, *94*(C11), 16,227–16,236. <https://doi.org/10.1029/JC094iC11p16227>
- Overduin, P. P., Liebner, S., Knoblauch, C., Günther, F., Wetterich, S., Schirrmeister, L., et al. (2015). Methane oxidation following submarine permafrost degradation: Measurements from a central Laptev Sea shelf borehole. *Journal of Geophysical Research: Biogeosciences*, *120*, 965–978. <https://doi.org/10.1002/2014JG002862>
- Overduin, P. P., Schneider von Deimling, T., Miesner, F., Grigoriev, M. N., Ruppel, C., Vasiliev, A., et al. (2019). Submarine permafrost map in the Arctic modeled using 1-D transient heat flux (supermap). *Journal of Geophysical Research: Oceans*, *124*, 3490–3507. <https://doi.org/10.1029/2018JC014675>
- Overduin, P. P., Westermann, S., Yoshikawa, K., Haberlau, T., Romanovsky, V., & Wetterich, S. (2012). Geoelectric observations of the degradation of nearshore submarine permafrost at Barrow (Alaskan Beaufort Sea). *Journal of Geophysical Research*, *117*, F02004. <https://doi.org/10.1029/2011JF002088>
- Overduin, P. P., Wetterich, S., Günther, F., Grigoriev, M. N., Grosse, G., Schirrmeister, L., et al. (2016). Coastal dynamics and submarine permafrost in shallow water of the central Laptev Sea, East Siberia. *The Cryosphere*, *10*(4), 1449. <https://doi.org/10.5194/tc-10-1449-2016>
- Rekant, P., Bauch, H. A., Schwenk, T., Portnov, A., Gusev, E., Spiess, V., et al. (2015). Evolution of subsea permafrost landscapes in Arctic Siberia since the late Pleistocene: A synoptic insight from acoustic data of the Laptev Sea. *Arktos*, *1*(1), 11. <https://doi.org/10.1007/s41063-015-0011-y>
- Riedel, M., Brent, T. A., Taylor, G., Taylor, A. E., Hong, J.-K., Jin, Y.-K., & Dallimore, S. R. (2017). Evidence for gas hydrate occurrences in the Canadian Arctic Beaufort Sea within permafrost-associated shelf and deep-water marine environments. *Marine and Petroleum Geology*, *81*, 66–78. <https://doi.org/10.1016/j.marpetgeo.2016.12.027>
- Romanovskii, N. N., Hubberten, H.-W., Gavrilov, A. V., Tumskey, V. E., & Kholodov, A. L. (2004). Permafrost of the East Siberian Arctic shelf and coastal lowlands. *Quaternary Science Reviews*, *23*(11–13), 1359–1369. <https://doi.org/10.1016/j.quascirev.2003.12.014>
- Romanovskii, N. N., Hubberten, H.-W., Gavrilov, A., Tumskey, V., Tipenko, G. S., Grigoriev, M., & Siegert, C. (2000). Thermokarst and land-ocean interactions, Laptev Sea Region, Russia. *Permafrost and Periglacial Processes*, *11*(2), 137–152. [https://doi.org/10.1002/1099-1530\(200004/06\)11:2<137::AID-PPP345>3.0.CO;2-L](https://doi.org/10.1002/1099-1530(200004/06)11:2<137::AID-PPP345>3.0.CO;2-L)
- Roy-Leveille, P., & Burn, C. R. (2017). Near-shore talik development beneath shallow water in expanding thermokarst lakes, Old Crow Flats, Yukon. *Journal of Geophysical Research: Earth Surface*, *122*, 1070–1089. <https://doi.org/10.1002/2016JF004022>
- Schell, D. M. (1974). Regeneration of nitrogenous nutrients in Arctic Alaskan estuarine waters. In J. C. Reed & J. E. Sater (Eds.), *The Coast and Shelf of the Beaufort Sea* (pp. 649–664). Arlington, Virginia: The Arctic Institute of North America.
- Schirrmeister, L., Grigoriev, M. N., Strauss, J., Grosse, G., Overduin, P. P., Kholodov, A., et al. (2018). Sediment characteristics of a thermokarst lagoon in the northeastern Siberian Arctic (Ivashkina Lagoon, Bykovsky Peninsula). *Arktos*, *4*(1), 13. <https://doi.org/10.1007/s41063-018-0049-8>
- Schirrmeister, L., Siegert, C., Kunitzky, V. V., Grootes, P. M., & Erlenkeuser, H. (2002). Late quaternary ice-rich permafrost sequences as a paleoenvironmental archive for the Laptev Sea region in northern Siberia. *International Journal of Earth Sciences*, *91*(1), 154–167. <https://doi.org/10.1007/s005310100205>
- Schuur, E. A. G., McGuire, A. D., Schädel, C., Grosse, G., Harden, J. W., Hayes, D. J., et al. (2015). Climate change and the permafrost carbon feedback. *Nature*, *520*(7546), 171–179. <https://doi.org/10.1038/nature14338>
- Schwaborn, G., Andreev, A., Rachold, V., Hubberten, H.-W., Grigoriev, M. N., Tumskey, V., et al. (2002). Evolution of Lake Nikolay, Arga Island, western Lena River Delta, during Late Pleistocene and Holocene time. *Polarforschung*, *70*, 69–82.
- Sellmann, P. V. (1989). Seafloor temperature and conductivity data from coastal waters of the US Beaufort Sea. US Army Corps of Engineers, Cold Regions Research & Engineering Laboratory (Vol. 89, No. 1).
- Sellmann, P. V., Delaney, A. J., & Arcone, S. A. (1989). Coastal submarine permafrost and bedrock observations using DC resistivity. U.S. Army Cold Regions Research and Engineering Laboratory (CRREL) Report, National Technical Information Service, Hanover, New Hampshire, 89-13.
- Shakhova, N., Semiletov, I., Gustafsson, O., Sergienko, V., Lobkovsky, L., Dudarev, O., et al. (2017). Current rates and mechanisms of subsea permafrost degradation in the East Siberian Arctic Shelf. *Nature Communications*, *8*, 15872. <https://doi.org/10.1038/ncomms15872>
- Shakhova, N., Semiletov, I., Salyuk, A., Yusupov, V., Kosmach, D., & Gustafsson, O. (2010). Extensive methane venting to the atmosphere from sediments of the East Siberian Arctic Shelf. *Science*, *327*(5970), 1246–1250. <https://doi.org/10.1126/science.1182221>
- Shampine, L. F., & Reichelt, M. W. (1997). The MATLAB ODE suite. *SIAM Journal on Scientific Computing*, *18*(1), 1–22.
- Solomon, S. M., Taylor, A. E., & Stevens, C. W. (2008). Nearshore ground temperatures, seasonal ice bonding, and permafrost formation within the bottom-fast ice zone, Mackenzie Delta, NWT. In *Proceedings of the Ninth International Conference on Permafrost, Fairbanks, Alaska 29* (pp. 1675–1680).

- Spangenberg, I., Overduin, P. P., Damm, E., Bussmann, I., Meyer, H., Liebner, S., et al. (2020). Methane pathways in winter ice of thermokarst lakes, lagoons and coastal waters in North Siberia. *The Cryosphere Discussions*, 2020, 1–28. <https://www.the-cryosphere-discuss.net/tc-2019-304/>
- Strauss, J., Boike, J., Bolshiyarov, D. Y., Grigoriev, M. N., El-Hajj, H., Morgenstern, A., et al. (2018). Russian-German Cooperation: Expeditions to Siberia in 2017, Berichte zur Polar- und Meeresforschung - Reports on polar and marine research, Bremerhaven, Alfred Wegener Institute for Polar and Marine Research, 725, 296 p. https://doi.org/10.2312/BzPM_0725_2018
- Strauss, J., Schirmer, L., Grosse, G., Wetterich, S., Ulrich, M., Herzschuh, U., & Hubberten, H.-W. (2013). The deep permafrost carbon pool of the Yedoma Region in Siberia and Alaska. *Geophysical Research Letters*, 40, 6165–6170. <https://doi.org/10.1002/2013GL058088>
- Swarzenski, P. W., Johnson, C. D., Lorenson, T. D., Conaway, C. H., Gibbs, A. E., Erikson, L. H., et al. (2016). Seasonal electrical resistivity surveys of a coastal bluff, Barter Island, North Slope Alaska: Seasonal electrical resistivity. *Journal of Environmental and Engineering Geophysics*, 21(1), 37–42. <https://doi.org/10.2113/JEEG21.1.37>
- Tweedley, J. R., Dittmann, S. R., Whitfield, A. K., Withers, K., Hoeksema, S. D., & Potter, I. C. (2019). Hypersalinity: Global distribution, causes, and present and future effects on the biota of estuaries and lagoons. *Coasts and estuaries*, 2019, 523–546. Elsevier. <https://doi.org/10.1016/B978-0-12-814003-1.00030-7>
- Ulyantsev, A. S., Bratskaya, S. Y., Romankevich, E. A., Semiletov, I. P., & Avramenko, V. A. (2016, March). Particle size composition of Holocene-Pleistocene deposits of the Laptev Sea (Buor-Khaya Bay). In *Doklady Earth Sciences* (Vol. 467, No. 1, pp. 241–245). Pleiades Publishing. <https://doi.org/10.1134/S1028334X16030168>
- Ulyantsev, A. S., Romankevich, E. A., Peresypkin, V. I., Belyaev, N. A., Semiletov, I. P., Bratskaya, S. Y., et al. (2016). Lignin as an indicator of the sedimentation conditions on the Arctic shelf. In *Doklady Earth Sciences* (Vol. 467, No. 1, pp. 264–269). Pleiades Publishing. <https://doi.org/10.1134/S1028334X16030089>
- Vonk, J. E., Sánchez-García, L., VanDongen, B. E., Alling, V., Kosmach, D., Charkin, A., et al. (2012). Activation of old carbon by erosion of coastal and subsea permafrost in Arctic Siberia. *Nature*, 489(7414), 137. <https://doi.org/10.1038/nature11392>
- Westermann, S., Langer, M., Boike, J., Heikenfeld, M., Peter, M., Eitzelmüller, B., & Krinner, G. (2016). Simulating the thermal regime and thaw processes of ice-rich permafrost ground with the land-surface model CryoGrid 3. *Geoscientific Model Development*, 9(2), 523. <https://doi.org/10.5194/gmd-9-523-2016>
- Westermann, S., Schuler, T. V., Gislén, K., & Eitzelmüller, B. (2013). Transient thermal modeling of permafrost conditions in southern Norway. *The Cryosphere*, 7(2), 719. <https://doi.org/10.5194/tc-7-719-2013>
- Wild, B., Shakhova, N., Dudarev, O., Ruban, A., Kosmach, D., Tumskey, V., et al. (2018). Organic matter across subsea permafrost thaw horizons on the East Siberian Arctic Shelf. *The Cryosphere Discussions*, 2018, 1–26. <https://www.the-cryosphere-discuss.net/tc-2018-229/>
- Williams, P. J., & Smith, M. W. (1991). *The Frozen Earth*. Cambridge: Cambridge University Press.
- Winkel, M., Mitzscherling, J., Overduin, P. P., Horn, F., Winterfeld, M., Rijkers, R., et al. (2018). Anaerobic methanotrophic communities thrive in deep submarine permafrost. *Scientific Reports*, 8(1), 1291. <https://doi.org/10.1038/s41598-018-19505-9>
- Winkel, M., Sepulveda-Jauregui, A., Martinez-Cruz, K., Heslop, J. K., Rijkers, R., Horn, F., et al. (2019). First evidence for cold-adapted anaerobic oxidation of methane in deep sediments of thermokarst lakes. *Environmental Research Communications*, 1(2), 021002. <https://doi.org/10.1088/2515-7620/ab1042>
- You, Y., Yu, Q., Pan, X., Wang, X., & Guo, L. (2017). Geophysical imaging of permafrost and talik configuration beneath a thermokarst lake. *Permafrost and Periglacial Processes*, 28(2), 470–476. <https://doi.org/10.1002/ppp.1938>

Erratum

Due to a typographical error, the maximum porewater salt concentrations in an unfrozen state for Scenario 3 and Scenario 6 models were incorrectly written as 495 and 741 mol/m³, respectively. In fact, the correct figures are 741 and 495 mol/m³. The error has been corrected, and this may be considered the official version of record.